International Journal of Mechanical Sciences 306 (2025) 110859

Contents lists available at ScienceDirect

International Journal of Mechanical Sciences

journal homepage: www.elsevier.com/locate/ijmecsci

Higher-order defective metamaterial for multi-band low-frequency vibration localization

Yupei Jian [a], Kexiang Wang [a], Cuipeng Xia [b,*], Deqing Huang [a], Hesheng Han [b], Guobiao Hu [c,*]

[a] School of Electrical Engineering, Southwest Jiaotong University, Chengdu, Sichuan 610031, China
[b] Department of Mechanical and Mechatronics Engineering, The University of Auckland, Auckland 1010, New Zealand
[c] Internet of Things Thrust, The Hong Kong University of Science and Technology (Guangzhou), Guangzhou, Guangdong 511400, China

ARTICLE INFO

Keywords:
Metamaterial
Wave manipulation
Band gap
Defect
Higher-order states
Multi-band energy localization

ABSTRACT

Defective metamaterials offer significant potential for applications in filtering, sensing, waveguiding, and energy harvesting, owing to defect states capable of localizing vibrational energy. However, constraints from Bragg scattering typically restrict these states to high-frequency ranges, and they are sparse within a single bandgap. Conventional strategies that add multiple defects broaden the spectrum but suffer from inter-defect dispersion that weakens energy concentration. In this study, a novel defective rhombic metamaterial (DRM) is proposed to achieve multi-band low-frequency defect states from a single-point defect. The novelty rests on two mechanisms: (1) the rhombic geometry's low effective stiffness significantly lowers the bandgap frequency without enlarging lattice size; and (2) the DRM supports higher-order defect states, enabling multiple localized modes to coexist within a single bandgap while maintaining strong localization. The band structures of the DRM are first analysed using finite element (FE) simulations, demonstrating the concept of low-frequency higher-order defect modes. Subsequently, the spectral element method (SEM) is employed to evaluate the transmittance characteristics, followed by parametric studies to explore the influence of geometric parameters on energy-localization behavior. Finally, the theoretical and numerical predictions are validated experimentally, providing the first experimental evidence of higher-order defect modes in the sub-kilohertz range. Overall, this work presents a promising strategy for broadband low-frequency energy localization using compact single-point-defect metamaterials, paving the way for higher power density in miniaturized energy harvesters and enhanced resolution in sensing applications.

1. Introduction

Phononic crystals (PnCs) and metamaterials have attracted widespread attention due to their exceptional ability to manipulate wave propagation through engineered periodic structures. A variety of unique wave phenomena have been extensively explored in these systems, including negative refraction [1–3], bandgap formation [4–6], topological edge states [7–9], and non-reciprocal wave propagation [10–12]. Among these phenomena, defect states are of particular interest for their ability to localize energy. Defect states refer to localized vibrational modes induced by intentional disruptions of the periodicity in PnCs/metamaterials [13,14]. These states emerge within bandgaps, as the structural defect functions as an energy trap, capturing vibrational energy that would otherwise be attenuated. The resulting confinement leads to standing waves and a significant amplification of vibrational energy at the defect site. Although similar to structural resonances, defect states have been shown to achieve much stronger energy localization [15–17]. As a result, defective PnCs and metamaterials have shown great potential in lots of applications, such as vibration filtering [18–21], sensing [22–25], waveguiding [26–29], and energy harvesting [30–34]. For instance, directional wave propagation was realized using line defects formed by removing scatterers [35]. Acoustic energy focusing with pressure amplification was achieved through Helmholtz-resonator-based defects [36], with transmission gains up to 30.83 mV/Pa.

Despite these promising prospects, defect states in PnCs and metamaterials face two major limitations. First, they typically emerge at relatively high frequencies, usually above several kilohertz [37–39]. For

* Corresponding authors.
E-mail addresses: cxia144@aucklanduni.ac.nz (C. Xia), guobiaohu@hkust-gz.edu.cn (G. Hu).

https://doi.org/10.1016/j.ijmecsci.2025.110859
Received 28 June 2025; Received in revised form 16 September 2025; Accepted 17 September 2025
Available online 18 September 2025

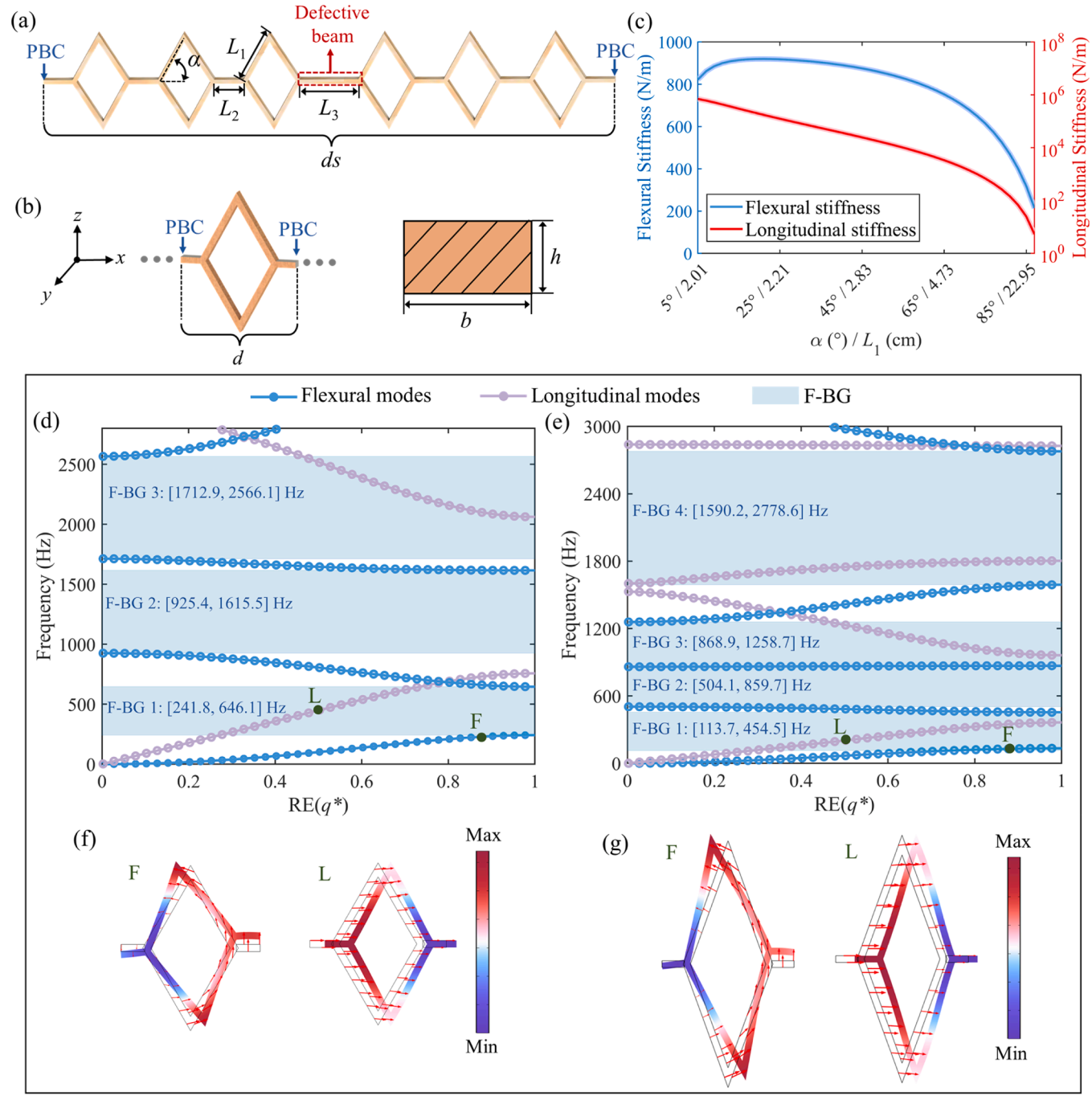

Fig. 1. (a) Schematic of the DRM with infinite configuration. "PBC" denotes the Floquet-Bloch periodic boundary condition; (b) Infinitely perfect rhombic metamaterial and the cross-section of the struts; (c) The effective stiffness of a rhombic unit with varying α and L_1. α varies from 5° to 85°, with $L_1 = 0.02/\cos(\alpha)$ to maintain a constant lattice constant $d = 6$ cm; (d) Band structure of the PRM. Blue curves with circular markers represent flexural modes, and purple curves with circular markers correspond to longitudinal modes. The flexural bandgaps are highlighted by blue-shaded regions; (e) Band structure of the PRM with modified L_1 and α; Mode shapes corresponding to the selected points (green dot) in (d) and (e) are shown in (f) and (g), respectively. F and L denote the flexural mode and longitudinal modes, respectively.

example, defect modes in the 20-60 kHz range have been reported in various scatterer-based PnC and metamaterial designs, such as those incorporating metallic cylindrical scatterers [40], embedded polygonal cavities [41], and structures with alternating sections of different materials [42]. The high-frequency nature of these defect modes is primarily attributed to the Bragg scattering mechanism, which underlies Bragg bandgaps and is formed only when the lattice constant is comparable to the wavelength [43]. Consequently, shifting defect modes to lower frequencies typically requires either impractically large structures or alternative design strategies. To target sub-kilohertz excitations commonly encountered in buildings, vehicles, and industrial machinery [44–46], locally resonant designs embed resonators in a metamaterial lattice and create defect sites by selectively removing resonators [16, 47]. This exploits subwavelength wave control to generate low-frequency defect states without increasing the unit-cell size, but the added resonator mass compromises suitability for lightweight applications.

Another challenge for defective PnCs and metamaterials is their

narrow operational bandwidth, which limits effectiveness in broadband vibration environments and multi-band localization tasks. To address this, researchers have proposed several strategies that generally fall into three categories. The first approach is defect-mode splitting, where a single defect mode is split into multiple modes to broaden the operational bandwidth. This can be realized by introducing dual structural defects [48–52] or by attaching a secondary resonator at the defect site [53]. However, arbitrarily adding defects does not necessarily produce additional defect states, and energy localization may weaken as defect sites compete. The second strategy is multi-bandgap defect engineering, in which defect states are independently created within distinct bandgaps. Examples include creating defect states separately in Bragg and locally resonant bandgaps [54], or in two locally resonant bandgaps governed by different mechanisms [55]. The third approach utilizes multiphysics coupling to realize reconfigurable defect states, thereby expanding the frequency coverage. This route typically involves smart materials such as piezoelectric [56–59] and magnetostrictive materials [60,61]. By applying external electric or magnetic fields, the effective stiffness of the defect structures can be actively tuned to control defect frequencies. In our recent work [62], we integrated multi-modal shunt resonant circuits into piezoelectric metamaterials to create "electrically controlled defects", enabling arbitrary and decoupled multi-band wave localization. Thermal loading at defect sites can also modify local stiffness through the stress-stiffening effect, thereby altering defect-mode behavior [49,63,64]. However, the above active tuning methods require external energy, which limits their use in passive applications such as energy harvesting or autonomous sensing.

In this study, we propose a novel defective rhombic metamaterial (DRM) capable of generating multiple low-frequency defect states through a single-point defect within a compact lattice. This structure consists of a periodic rhombic-like truss made of slender beams, where the defect is introduced by locally modifying the dimensions of a connecting beam. For ease of differentiation, the uniform-cell counterpart is termed the perfect rhombic metamaterial (PRM). Truss metamaterials have garnered considerable attention for their low-frequency bandgaps effect, largely attributed to their concave geometries [65,66]. Representative configurations include X-shaped [67,68], rhombic [69,70], pentagram [71,72], and hexagonal designs [73]. These structures combine high strength with low weight, ideal for load-bearing yet lightweight applications [74]. As the basic components of truss metamaterials, beams and rods have been extensively investigated for their mechanical behavior [75–77]. To capture the dynamics of truss periodic units, common modeling methods include the finite element method (FEM) [78], the transfer matrix method (TMM) [79], and the spectral element method (SEM) [69,80]. Among them, TMM may suffer numerical instability at high frequencies due to the successive multiplication of transfer matrices, particularly in systems with massive substructures [81]. FEM, while more stable, becomes computationally expensive as the structural scale increases [82,83]. In contrast, SEM improves stability and efficiency by constructing global matrices with a minimal number of degrees of freedom [84,85], making it especially suitable for analyzing complex periodic systems such as truss metamaterials.

Building on the low-frequency characteristics of truss metamaterials, this work embeds a single defect into a compact rhombic lattice to generate low-frequency defect states (here, "low-frequency" specifically refers to the sub-kilohertz range). This approach achieves low-frequency operation without resorting to large structures or significant added mass. To broaden the defect-mode frequency range, we pioneer the concept of higher-order defect states, defined as a sequence of distinct, spatially localized modes within a single Bragg bandgap, each tied to a successive eigenmode of the defect element. Unlike the conventional defect-mode splitting [48,49,52] or multi-bandgap defect approaches [54,55], which depend primarily on the fundamental resonance and require multiple defect sites, our approach exploits multiple higher-order modes at a single defect site to localize flexural waves inside one bandgap. This mechanism substantially improves bandgap utilization while the single-point defect reduces structural design complexity. In what follows, we demonstrate the feasibility of exciting higher-order defect states via the defect's higher-order flexural modes, validate the concept through modal analysis, and compare our design against existing multi-defect-mode architectures to highlight its simplicity and performance advantages.

This paper is organized as follows. Section 2 details the DRM design and analyzes its multiple low-frequency defect bands through band structure analysis. Section 3 introduces the dynamic model of the DRM based on the SEM. In Section 4, the multi-band low-frequency energy localization induced by defect states is systematically analyzed using both SEM and FE models. Section 5 experimentally validates the accuracy of the theoretical and simulation results and confirms the formation of low-frequency higher-order defect states. Finally, Section 6 provides concluding remarks.

2. Design and mechanism of the defective rhombic metamaterials

This section presents a framework utilizing a rhombic-shaped truss structure to effectively lower and broaden the frequency range of defect states. Section 2.1 details the geometry of the proposed DRM. Section 2.2 presents band structure analyses showing low-frequency bandgaps and defect modes, and demonstrates how higher-order defect state mechanisms increase defect-mode density to enable broadband wave localization in the sub-kilohertz regime.

2.1. System configuration

The proposed DRM structure comprises n unit cells arranged periodically, each featuring a rhombus-shaped substructure, as shown in Fig. 1(a). In the global coordinate system, each substructure consists of six uniform, isotropic elastic beams. The inclined beams forming the rhombus have length L_1 and are oriented at an angle α with respect to the x-axis, while the horizontal connecting beams have length L_2. All beam elements share identical cross-sectional dimensions, with width b and thickness h, as shown in Fig. 1(b). A structural defect is introduced by changing the length of one connecting beam to L_3, which breaks the periodicity and disrupts the physical mechanism of bandgap formation. Such asymmetry induces localized defect modes inside the bandgap. By adjusting the defect geometry, the mode confined around the defect site can be tailored, allowing exploration of low-frequency and broadband wave localization behavior. In addition, Fig. 1(b) presents the PRM in its infinite configuration, used as a reference to verify the conditions for defect mode generation.

2.2. Defect-band analysis

This subsection investigates the defect-band properties of the DRM using band structure analysis. The relation between circular frequency ω and wavenumber q, commonly referred to as the band structure, is a fundamental tool for characterizing wave propagation in periodic systems. To investigate the formation of defect states for different wave

Table 1
Material and geometric properties of the DRM and PRM.

L_1(cm)	L_2(cm)	L_3(cm)	α(°)	b(cm)	h(cm)	E(Gpa)	ρ(kg/m^3)	ν
4	2	4	60	0.5	0.3	2.2e9	1100	0.394

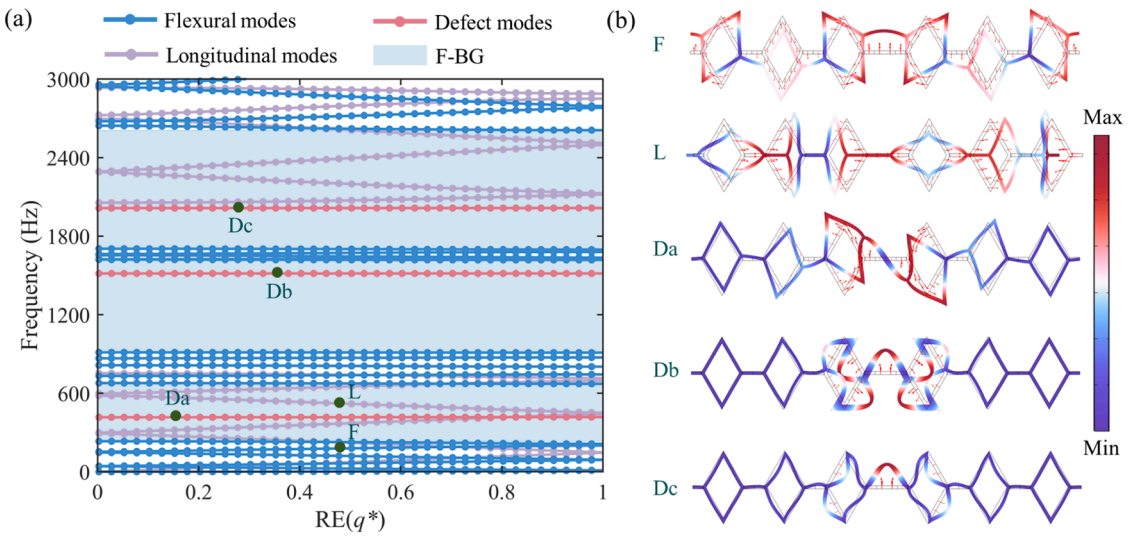

Fig. 2. (a) Band structure of the DRM. Blue curves with circular markers represent flexural modes, and purple curves with circular markers correspond to longitudinal modes. The flexural bandgaps are highlighted by blue-shaded regions. Three defect bands are shown as red curves with circular markers; (b) Mode shapes corresponding to the selected points (green dot) in (a).

polarizations, their low-frequency properties, and mode-localization behavior in the proposed DRM, band structure analysis is conducted using COMSOL Multiphysics. Two periodically constrained configurations are considered: PRM (Case 1) and DRM (Case 2). For each case, the band structures of the above models are derived by computing the eigenfrequencies ω over a range of wavenumbers q. Material and geometric parameters are summarized in Table 1, where the lattice constant d is only 6 cm, consistent with the compact design described earlier.

In Case 1, Floquet-Bloch periodic boundary conditions are applied to the cross sections of the left and right ends of the rhombic unit cell, as illustrated in Fig. 1(b). The resulting band structure is presented in Fig. 1(d). Re(q^*) denotes the real part of the dimensionless wavenumber $q^* = qd/\pi$. The blue and purple curves in Fig. 1(d) represent the flexural and longitudinal modes, respectively, and the corresponding mode shapes at selected points (green dots) are provided in Fig. 1(f). It can be observed that the PRM exhibits three flexural bandgaps (blue-shaded regions) in the frequency ranges of 241.8 Hz-646.1 Hz, 925.4 Hz-1615.5 Hz, and 1712.9 Hz-2566.1 Hz, corresponding to the first-, second-, and third-order Bragg scattering mechanisms, respectively. A first-order longitudinal bandgap appears at a higher frequency range of 757.4-2061.6 Hz, reflecting the structure's greater axial stiffness compared to its bending stiffness. Notably, the overlapping frequency region between the flexural and longitudinal bandgaps constitutes a complete (omnidirectional) bandgap [86], in which propagation of both flexural and longitudinal waves is suppressed.

It is important to note that the center frequency of the first-order flexural bandgap is relatively low, and significantly lower than that of conventional Bragg-type metamaterials with comparable lattice constants, which typically fall within the range of 20 kHz-60 kHz [40–42]. Such sub-kilohertz Bragg bandgaps have also been observed numerically and experimentally in other truss-type metamaterials employing similar polymeric materials and centimetre-scale lattice constants [65,80,87]. Actually, many studies have lowered Bragg-type bandgap frequencies through topology optimization [88,89], by adding concentrated masses to reduce eigenfrequencies [90], or by embedding of acoustic inclusions (e.g., sonic-black-hole structures) to reduce the unit-cell effective sound speed [91]. To explain the low-frequency Bragg bandgaps observed here, we invoke the Bragg scattering condition that governs bandgap formation, given by [92]:

$$2d = N\lambda (N = 1, 2, \ldots), \tag{1}$$

where λ is the wavelength and N denotes the bandgap order. For flexural waves propagating in beam structures, by incorporating the relationship between wave velocity and frequency, the center frequency of the first-order flexural bandgap can be estimated as follows:

$$f_{\text{Bragg}} \approx \frac{1}{2d^2}\sqrt{\frac{EI_{\text{eff}}}{\rho A}}, \tag{2}$$

where EI_{eff} and ρA represent the effective stiffness and the mass density, respectively. Due to the rhombic geometry, the effective stiffness of the unit cell differs from that of a simple straight beam and can be tuned by L_1 and α. According to Eq. (2), the bandgap center frequency varies with the effective stiffness EI_{eff} when the lattice constant d and mass density ρA are held fixed. To illustrate this effect, $L_1 = 5.85$ cm and $\alpha = 70^\circ$ are selected, while keeping $d = 6$ cm. The resulting band structure in Fig. 1(e) shows a downward shift in the first flexural bandgap to the range of 113.7 Hz-454.5 Hz. Corresponding mode shapes at selected points (green dots) are plotted in Fig. 1(g).

To quantify how L_1 and α affect the effective stiffness, COMSOL simulations are conducted to estimate the flexural and longitudinal stiffness of a rhombic unit for a variety of geometries. In the Solid Mechanics module, one end of the rhombic unit is fixed, while a unit force is applied either perpendicular or parallel to the connecting beam at the other end. A static study is used to evaluate the stiffness. The angle α varies from 5° to 85°, and L_1 is adjusted accordingly using $L_1 = 0.02/\cos(\alpha)$ to maintain a constant lattice constant $d = 6$ cm. As shown in Fig. 1(c), the flexural stiffness slightly increases at small α, then gradually decreases, whereas the longitudinal stiffness decreases consistently with increasing α. This behavior explains the lower bandgap frequencies observed in Fig. 1(e) for the identical lattice constant. In summary, these findings confirm that the rhombic metamaterial can sustain low-frequency bandgaps with compact lattice constants, thereby providing the foundation for the low-frequency defect modes explored in this study.

In Case 2, a supercell approach is employed to capture defect bands induced by the DRM. A supercell composed of six units is considered, where the connecting beam between the third and fourth cells is modified to L_3 to introduce a defect, thereby breaking the translational symmetry along the beam direction. Floquet-Bloch boundary conditions are applied at the ends of the supercell, as illustrated in Fig. 1(a). Material and geometric parameters are used in Table 1, and the modified lattice constant is $ds = 38$ cm. The resulting band structure, shown in

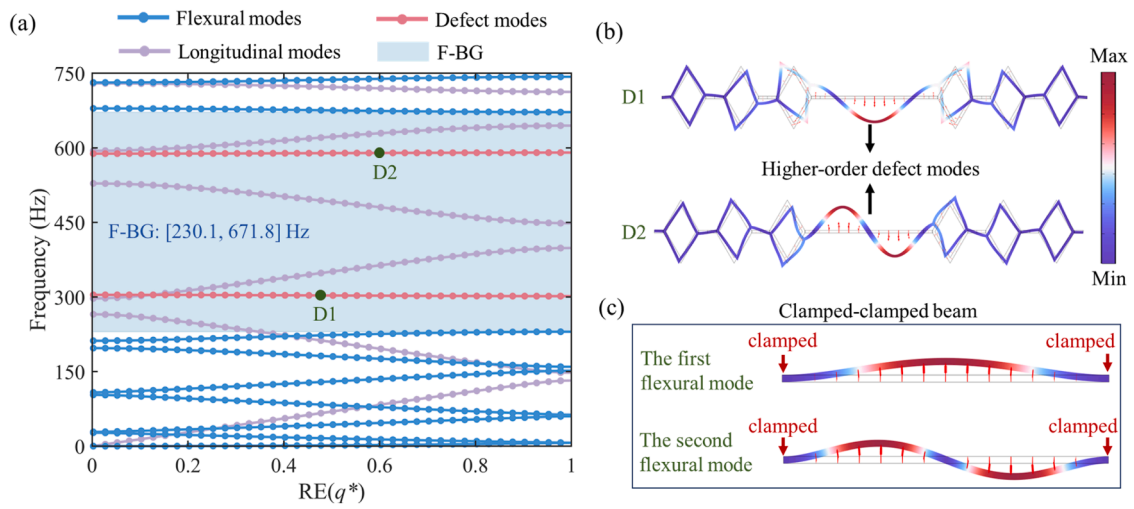

Fig. 3. (a) Band structure of the DRM with higher-order defect states. Blue curves with circular markers represent flexural modes, while purple curves with circular markers correspond to longitudinal modes. Higher-order defect bands are shown as red curves with circular markers; (b) Mode shapes corresponding to the selected points (green dot) in the band structure; (c) Reference first- and second-order flexural modes of a clamped-clamped beam computed by FE.

Fig. 2(a), contains significantly more dispersion branches than in Fig. 1(a). This increase arises from band folding introduced by the supercell configuration, which compresses the dispersion curves into a smaller Brillouin zone and thereby generates additional bands [93], while the bandgap ranges remain largely unchanged. Importantly, the change in L_3 breaks the PRM's translational symmetry and locally disrupts the mechanism responsible for bandgap formation. Consequently, pass-bands (i.e., defect bands) appear within each of the original multiple bandgaps, as indicated by the red curves marked with circles. These bands are nearly flat, meaning their slopes and thus their group velocities are close to zero. At these frequencies, wave propagation is strongly suppressed, and energy becomes confined near the defect. As a result, standing-wave-like modes emerge at the defect site, leading to significantly amplified local vibration amplitudes.

To gain more insight into the defect state characteristics, Fig. 2(b) presents mode shapes of representative defect states Da, Db, and Dc. From which the following observations are made: (1) wave localization and energy confinement are evident in Da-Dc, with vibrational energy concentrated around the spatial defect. In contrast, the reference flexural mode F exhibits a distributed energy profile. Such localization indicates potential for waveguiding, sensing, and narrow-band filtering applications; (2) these defect states originate from flexural coupling between the defective elements and the periodic host, as evidenced by their exclusive appearance within the flexural bandgaps (first- through third-order Bragg scattering). No defect modes occur in the longitudinal bandgap. Two factors explain the observed behavior. On the one hand, longitudinal (in-plane) waves couple weakly to the lattice periodicity and therefore tend to transmit rather than localize. On the other hand, beam theory predicts that changes in L_3 affect axial stiffness far less than bending stiffness, and consequently, symmetry breaking induced by beam-length variation is weak for axial excitations; (3) the rhombic cell design supports low-frequency localization, with the defect state in the first-order flexural bandgap occurring at approximately 418.1 Hz when $q^* = 1$. Beyond the above findings, the modal shapes of Da-Dc reveal distinct energy localization patterns. Specifically, the Da mode exhibits a dipole-like localization pattern [94], with peak strain odd-symmetrically distributed on both sides of the defect center and in opposite phases. In contrast, Db and Dc modes show monopole-like distributions [95], characterized by a single strain maximum at the defect center. This variation implies that, for applications such as energy harvesting or sensing, the placement of transduction elements should be tailored to the mode shape to avoid phase cancellation and ensure optimal performance.

It should be noted that wave propagation within a defect band typically exhibits near-zero group velocity, resulting in sharp, narrow-band frequency responses that limit practical use. Although the multiple defect states shown in Fig. 2(a) expand the localization bandwidth, they lie in separate bandgaps and only the first occurs at relatively low frequencies. Broadband localization is ideally achieved by introducing multiple defect states within the first-order bandgap. To this end, Fig. 3(a) presents the band structure of the DRM for $L_3 = 14$ cm, with all other parameters listed in Table 1. For clarity, we focus on the characteristics of the defect states within the first-order flexural bandgap. Two defect bands, denoted by red curves with circular markers, emerge at 301.6 Hz and 588.3 Hz. The selected mode shapes, labeled as D1 and D2, are shown in Fig. 3(b), clearly indicating energy confinement around the defective beam. Interestingly, the energy concentration regions in D1 and D2 resemble the first- and second-order flexural modes of a clamped-clamped beam, respectively. To further verify this correspondence, Fig. 3(c) presents FE eigenmode calculations for a beam under clamped-clamped boundary conditions with the same material and geometric parameters as the defective beam in Fig. 3(b). It can be seen that the clamped-clamped beam's first and second flexural mode shapes closely match the localized energy-concentration patterns observed at the defect site in the DRM.

Based on this observation, we hypothesize that the formation of defect states is influenced not only by the coupling between the defect and the periodic host (i.e., as illustrated in Fig. 2(a)), but also by the defect's intrinsic dynamics. The appearance of multiple defect bands in Fig. 3(a) can be attributed to the following mechanism: as the length of the defective beam L_3 increases, its flexural eigenfrequencies shift downward and become more closely spaced. When one or more of these eigenfrequencies fall inside the bandgap, they cannot couple to propagating Bloch modes and therefore localize around the defect. Accordingly, we identify the defect states shown in D1 and D2 as the higher-order defect states. It is important to emphasize that, in terms of formation mechanism and structural design, these higher-order defect states differ fundamentally from existing dual-defect or multi-bandgap defect designs. Specifically: (1) In dual-defect designs [48,49,52], coupling between the two defects splits originally coincident resonances into two distinct frequencies. Multi-bandgap defect designs, on the other hand, generate defect states by creating separate bandgaps through distinct mechanisms, each supporting a single defect mode. For example, [55] employs the mechanical and acoustic resonances of Helmholtz resonators to produce defect modes in two distinct bandgaps. However, these approaches still primarily rely on the defect's first-order

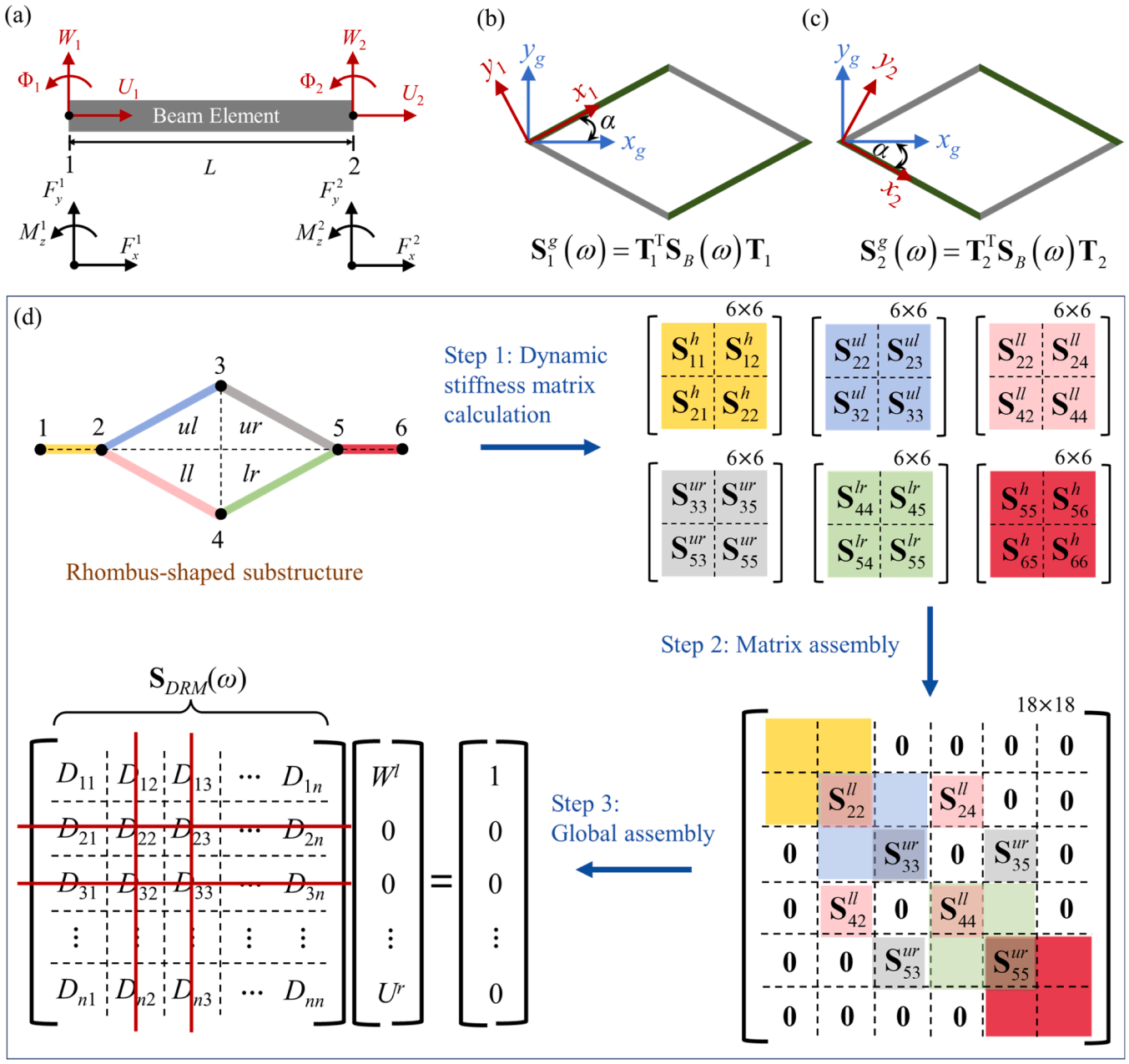

Fig. 4. (a) Spectral beam element in the local coordinate system; (b) Transformation from the local coordinate system x_1-y_1 to the global coordinate system x_g-y_g for the upper left and lower right beam elements; (c) Transformation from the local coordinate system x_2-y_2 to the global coordinate system x_g-y_g for the lower left and upper right beam elements; (d) Assembly procedure of the global dynamic stiffness matrix $\mathbf{S}_{DRM}(\omega)$ in the DRM.

modes. (2) To achieve multiple defect states, the aforementioned methods require introducing two or more defects into the periodic structure. In contrast, the design in this work leverages the higher-order defect state mechanism, enabling a single defect to produce multiple defect states within a single bandgap, thereby significantly enhancing design flexibility.

In summary, the preceding band structure analysis highlights the proposed DRM's advantage in achieving broadband low-frequency defect states. However, because dispersion analysis based on the finite-element method is computationally expensive and less effective at capturing the frequency-response characteristics of localized defect states, a dynamic model of a finite-length DRM is proposed in the following section.

3. Spectral element method

This section develops a dynamic model of the proposed DRM using the spectral element method (SEM). SEM ensures high accuracy while offering greater computational efficiency by reducing the number of element nodes. The elemental dynamic stiffness for the beam-like unit is derived, and the procedure for assembling the DRM's global dynamic matrix is introduced.

3.1. Derivation of the dynamic stiffness matrix

The analysis is conducted under the assumption of small elastic deflections [96,97], meaning that transverse displacements are much smaller than the beam length and axial strains remain within the linear elastic range. Under these conditions, geometric nonlinearities such as

stretching-induced bending and mid-plane stretching can be neglected, allowing transverse and axial vibrations to be treated as uncoupled. Consequently, the partial differential equation governing the motion of the beam element can be expressed as follows [69]:

$$\begin{cases} \rho A\dfrac{\partial^2 w(x,t)}{\partial t^2}+\kappa GA\left[\dfrac{\partial \phi(x,t)}{\partial x}-\dfrac{\partial^2 w(x,t)}{\partial x^2}\right]=0 \\ \rho I\dfrac{\partial^2 \phi(x,t)}{\partial t^2}+\kappa GA\left[\phi(x,t)-\dfrac{\partial w(x,t)}{\partial x}\right]-EI\dfrac{\partial^2 \phi(x,t)}{\partial x^2}=0 \\ \rho A\dfrac{\partial^2 u(x,t)}{\partial t^2}-EA\dfrac{\partial^2 u(x,t)}{\partial x^2}=0, \end{cases} \tag{3}$$

where $w(x,t)$, $\phi(x,t)$and $u(x,t)$ represent the transverse, rotational, and longitudinal displacements, respectively. E and G are the Young's modulus and shear modulus, respectively, which are related by $G = E/[2(1+\upsilon)]$, where υ is the Poisson's ratio. ρ denotes the mass density, $A = b\times h$ is the cross-sectional area, and I is the area moment of inertia. $\kappa$is the shear correction factor depending on the shape of the cross-section. Considering the DRM structure under harmonic excitation, the steady-state displacement solution in Eq. (3) can be expressed as:

$$\begin{cases} w(x,t)=W(x)e^{i\omega t} \\ \phi(x,t)=\Phi(x)e^{i\omega t} \\ u(x,t)=U(x)e^{i\omega t}. \end{cases} \tag{4}$$

By substituting Eq. (4) into Eq. (3) and eliminating the time-harmonic dependence $e^{i\omega t}$, the motion equation in the frequency domain is obtained as:

$$\begin{cases} -\omega^2\rho AW(x)+\kappa GA\left(\dfrac{d\Phi(x)}{dx}-\dfrac{d^2W(x)}{dx^2}\right)=0 \\ -\omega^2\rho I\Phi(x)+\kappa GA\left[\Phi(x)-\dfrac{dW(x)}{dx}\right]-EI\dfrac{d^2\Phi(x)}{\partial x^2}=0 \\ -\omega^2\rho AU(x)-EA\dfrac{d^2U(x)}{dx^2}=0. \end{cases} \tag{5}$$

Assuming the general solution to Eq. (5) is:

$$\begin{cases} W(x)=Ae^{ikx} \\ \Phi(x)=rAe^{ikx} \\ U(x)=\overline{A}e^{ikx}, \end{cases} \tag{6}$$

where A, r, and $\overline{A}$ are to-be-determined coefficients depending on the nodal displacements. By substituting Eq. (6) into Eq. (5) and solving the eigenvalue problem, the general solution in Eq. (6) can be rewritten as:

$$\begin{cases} W(x)=A_1e^{-ik_1x}+A_2e^{ik_1x}+A_4e^{-ik_2x}+A_5e^{ik_2x} \\ \Phi(x)=r_1A_1e^{-ik_1x}-r_1A_2e^{ik_1x}+r_2A_4e^{-ik_2x}-r_2A_5e^{ik_2x} \\ U(x)=A_3e^{-ik_3x}+A_6e^{ik_3x}, \end{cases} \tag{7}$$

where $r_p = -i\left(k_p^2-\frac{\omega^2\rho}{\kappa G}\right)/k_p$, $p=1$ or 2, and the wavenumber k_1, k_2, and k_3 are expressed as:

$$\begin{cases} k_1=\dfrac{k_F}{\sqrt{2}}\sqrt{\eta k_F^2+\sqrt{\eta^2k_F^4+4\left(1-\eta_1k_G^4\right)}} \\ k_2=\dfrac{k_F}{\sqrt{2}}\sqrt{\eta k_F^2-\sqrt{\eta^2k_F^4+4\left(1-\eta_1k_G^4\right)}} \\ k_3=\omega\sqrt{\dfrac{\rho}{E}}, \end{cases} \tag{8}$$

where $k_F=\left(\frac{\omega^2\rho A}{EI}\right)^{\frac{1}{4}}$, $k_G=\left(\frac{\omega^2\rho}{\kappa G}\right)^{\frac{1}{4}}$, $\eta=\frac{I}{A}+\frac{EI}{\kappa GA}$ and $\eta_1=\frac{I}{A}$. By substituting the nodal coordinates $[W_1\Phi_1U_1W_2\Phi_2U_2]$ into Eq. (7), the nodal displacements can be determined as:

$$\underbrace{\begin{bmatrix} W(0)\\ \Phi(0)\\ U(0)\\ W(L)\\ \Phi(L)\\ U(L) \end{bmatrix}}_{\mathbf{d}} = \underbrace{\begin{bmatrix} 1 & 1 & 0 & 1 & 1 & 0\\ r_1 & -r_1 & 0 & r_2 & -r_2 & 0\\ 0 & 0 & 1 & 0 & 0 & 1\\ e^{-ik_1L} & e^{ik_1L} & 0 & e^{-ik_2L} & e^{ik_2L} & 0\\ r_1e^{-ik_1L} & -r_1e^{ik_1L} & 0 & r_2e^{-ik_2L} & -r_2e^{ik_2L} & 0\\ 0 & 0 & e^{-ik_3L} & 0 & 0 & e^{ik_3L} \end{bmatrix}}_{\mathbf{R}} \underbrace{\begin{bmatrix} A_1\\ A_2\\ A_3\\ A_4\\ A_5\\ A_6 \end{bmatrix}}_{\mathbf{A}}. \tag{9}$$

Note that the transverse shear force, bending moment, and longitudinal force are distributed along the beam element in the following forms:

$$\begin{cases} F_y=\kappa GA\left[\dfrac{dW(x)}{dx}-\Phi(x)\right] \\ M_z=EI\dfrac{d\Phi(x)}{dx} \\ F_x=EA\dfrac{dU(x)}{dx}. \end{cases} \tag{10}$$

In other words, the nodal forces of a beam element can be expressed in terms of its nodal displacements. As illustrated in Fig. 4(a), nodes 1 and 2 correspond to the left and right ends, respectively. The subscripts x, y, and z denote the coordinate axes associated with the corresponding nodal forces. Substituting the nodal forces $\left[F_y^1M_z^1F_x^1F_y^2M_z^2F_x^2\right]$ into Eq. (7) yields:

$$\underbrace{\begin{bmatrix} -F_y(0)\\ -M_z(0)\\ -F_x(0)\\ F_y(L)\\ M_z(L)\\ F_x(L) \end{bmatrix}}_{\mathbf{f}} = \underbrace{\begin{bmatrix} -\kappa GA(-ik_1-r_1) & -\kappa GA(ik_1+r_1) & 0 & -\kappa GA(-ik_2-r_2) & -\kappa GA(-ik_2+r_2) & 0\\ iEIr_1k_1 & iEIr_1k_1 & 0 & iEIr_2k_2 & iEIr_2k_2 & 0\\ 0 & 0 & iEAk_3 & 0 & 0 & -iEAk_3\\ \kappa GA(-ik_1-r_1)e^{-ik_1L} & \kappa GA(ik_1+r_1)e^{ik_1L} & 0 & \kappa GA(-ik_2-r_2)e^{-ik_2L} & \kappa GA(ik_2+r_2)e^{ik_2L} & 0\\ -iEIr_1k_1e^{-ik_1L} & -iEIr_1k_1e^{ik_1L} & 0 & -iEIr_2k_2e^{-ik_2L} & -iEIr_2k_2e^{ik_2L} & 0\\ 0 & 0 & -iEAk_3e^{-ik_3L} & 0 & 0 & iEAk_3e^{ik_3L} \end{bmatrix}}_{\mathbf{H}} \underbrace{\begin{bmatrix} A_1\\ A_2\\ A_3\\ A_4\\ A_5\\ A_6 \end{bmatrix}}_{\mathbf{A}}. \tag{11}$$

Combining Eqs. (9) and (11) allows the representation of nodal force and moment in terms of the nodal displacements as:

$$\mathbf{f}=\mathbf{HR}^{-1}\mathbf{d}. \tag{12}$$

The frequency-dependent dynamic stiffness matrix of the beam element is given as $\mathbf{S}_B(\omega)=\mathbf{HR}^{-1}$.

3.2. Assembly of the dynamic stiffness matrix

In this subsection, the assembly of the global dynamic stiffness matrix for the DRM structure is described, from which its dynamic characteristics are obtained. It is important to note that $\mathbf{S}_B(\omega)$ is derived from the local coordinate system and must first be transformed into the global

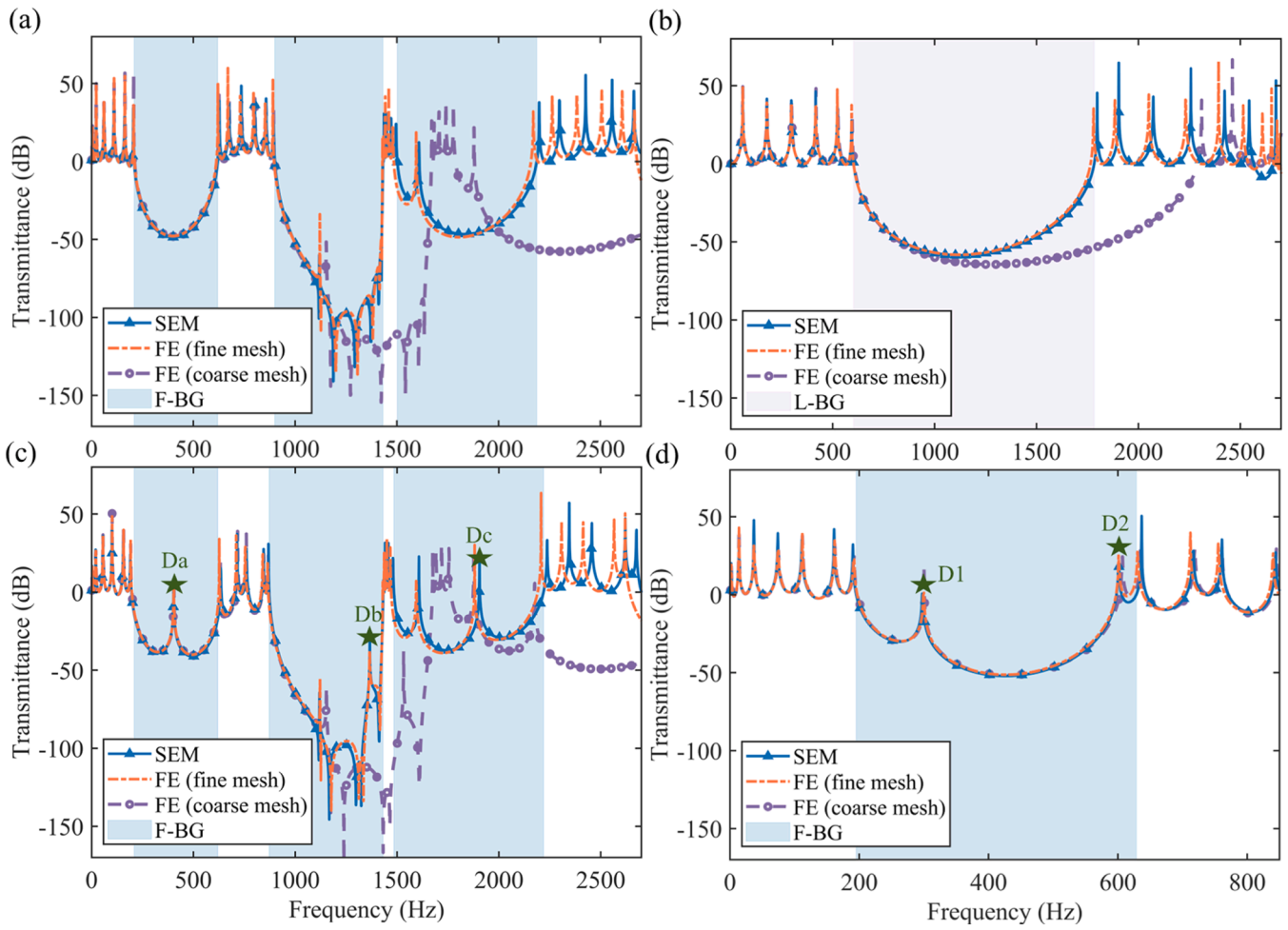

Fig. 5. (a) Transmittance of the PRM under flexural vibration; (b) Transmittance of the PRM under longitudinal vibration; (c) Transmittance of the DRM with $L_3 = 4$ cm under flexural vibration; (d) Transmittance of the DRM with $L_3 = 14$ cm under flexural vibration. In all cases, results are compared among SEM, fine mesh, and coarse mesh FE simulations.

coordinate system to construct the stiffness matrix of the rhombus-shaped substructure. The relationship between the two beam elements forming the upper left and lower right sides of the rhombus substructure and the global coordinate system is illustrated in Fig. 4(b). Based on geometric relations, $\mathbf{S}_B(\omega)$ in the x_1-y_1 coordinate system undergoes the following transformation to obtain its global counterpart $\mathbf{S}_1^g(\omega)$:

$$\mathbf{S}_1^g(\omega) = \mathbf{T}_1^{\mathrm{T}} \mathbf{S}_B(\omega) \mathrm{T}_1, \tag{13}$$

where $\mathbf{T}_1$ is the transformation matrix, expressed as:

$$\mathbf{T}_1 = \begin{bmatrix} \cos(\alpha) & 0 & \sin(\alpha) & 0 & 0 & 0 \\ 0 & 1 & 0 & 0 & 0 & 0 \\ -\sin(\alpha) & 0 & \cos(\alpha) & 0 & 0 & 0 \\ 0 & 0 & 0 & \cos(\alpha) & 0 & \sin(\alpha) \\ 0 & 0 & 0 & 0 & 1 & 0 \\ 0 & 0 & 0 & -\sin(\alpha) & 0 & \cos(\alpha) \end{bmatrix}. \tag{14}$$

Similarly, for the beam elements located at the lower left and upper right sides of the rhombus substructure, their coordinate system relationships are illustrated in Fig. 4(c). $\mathbf{S}_B(\omega)$ in the x_2-y_2 coordinate system transforms:

$$\mathbf{S}_2^g(\omega) = \mathbf{T}_2^{\mathrm{T}} \mathbf{S}_B(\omega) \mathrm{T}_2, \tag{15}$$

where $\mathbf{T}_2$ is the transformation matrix, given as follows:

$$\mathbf{T}_2 = \begin{bmatrix} \cos(\alpha) & 0 & -\sin(\alpha) & 0 & 0 & 0 \\ 0 & 1 & 0 & 0 & 0 & 0 \\ \sin(\alpha) & 0 & \cos(\alpha) & 0 & 0 & 0 \\ 0 & 0 & 0 & \cos(\alpha) & 0 & -\sin(\alpha) \\ 0 & 0 & 0 & 0 & 1 & 0 \\ 0 & 0 & 0 & \sin(\alpha) & 0 & \cos(\alpha) \end{bmatrix}. \tag{16}$$

For beam elements aligned with (x_g-y_g), no coordinate transformation is required. Subsequently, the global stiffness matrix $\mathbf{S}_{DRM}(\omega)$ of the DRM can then be assembled based on the finite element assembly procedure, which is graphically illustrated in Fig. 4(d). A representative rhombus-shaped substructure, consisting of six nodes labeled 1 through 6, is selected for demonstration. The four inclined beams, denoted by the superscripts *ur, ul, ll*, and *lr*, and oriented toward the four diagonal directions of the rhombus center, are modeled using Eqs. (13) and (15). The superscript *h* indicates connecting beams. Based on the nodal connectivity in Fig. 4(d), the stiffness matrix of the rhombus-shaped substructure can be assembled. By further considering periodicity, $\mathbf{S}_{DRM}(\omega)$ can be obtained.

In this study, a cantilever boundary condition is applied, where the left end of the DRM is clamped to a fixture and subjected to a unit force, while the right end remains free. Under this configuration, both rotational and longitudinal displacements at the clamped end are constrained to zero. The governing equation for the finite-length DRM is given as:

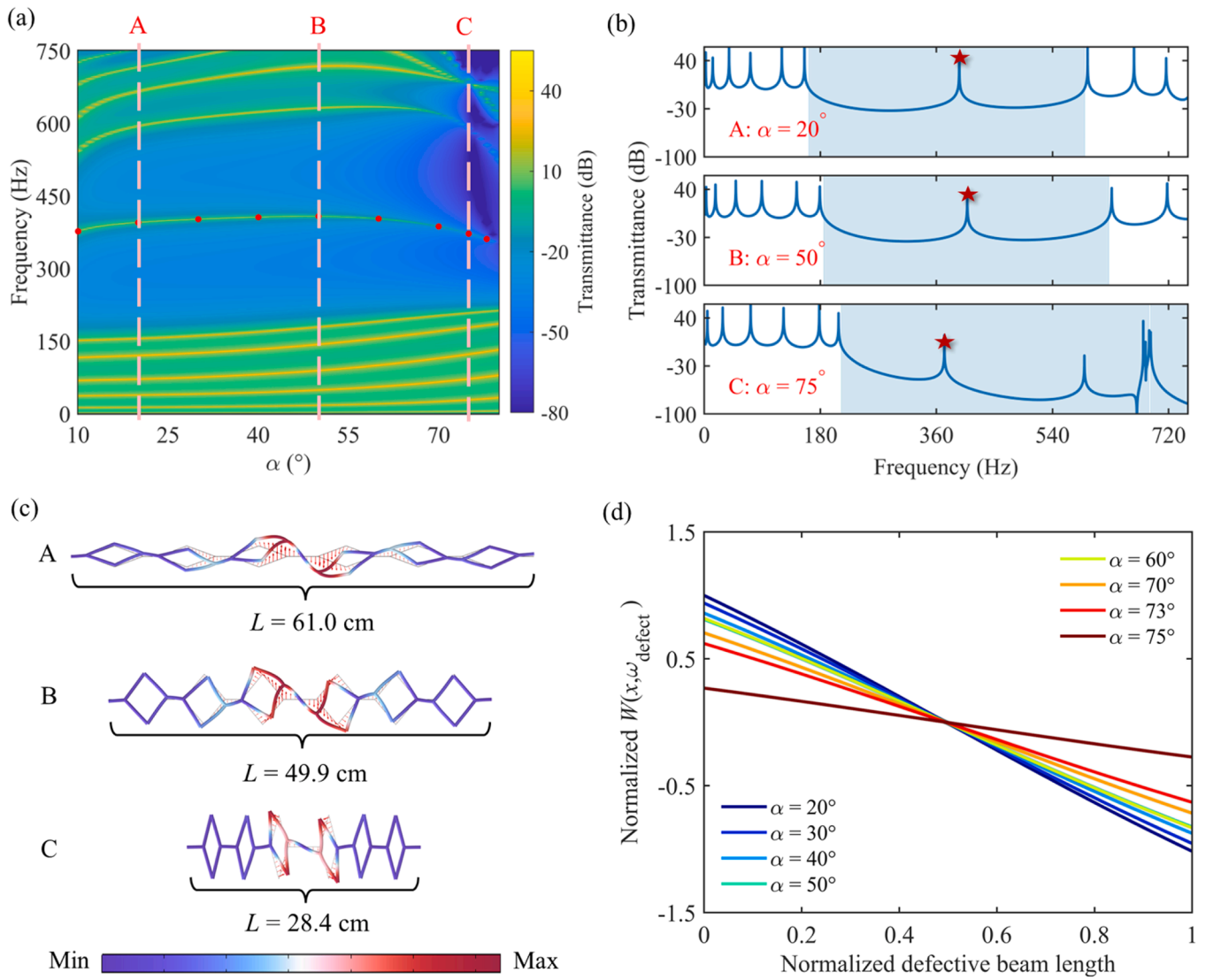

Fig. 6. (a) Heatmap of the DRM's transmittance versus α (10°-80°), with defect-state peak marked by red dots; (b) Transmittance curves for slices A, B, and C in (a), with defect-state peaks highlighted by red pentagrams; (c) Mode shapes at the defect-state peak frequency for cases A, B and C, with the total DRM length L indicated; (d) The variation of the normalized vibration amplitude of the defective beam at the defect-state frequency with changing α.

$$\mathbf{S}_{DRM}(\omega)\begin{bmatrix} W^l \\ \Phi^l = 0 \\ U^l = 0 \\ \vdots \\ W^r \\ \Phi^r \\ U^r \end{bmatrix} = \begin{bmatrix} 1 \\ 0 \\ 0 \\ \vdots \\ 0 \\ 0 \\ 0 \end{bmatrix}. \tag{17}$$

where the superscripts l and r refer to the nodes located at the leftmost and rightmost ends of the structure, respectively. Given that $\Phi^l = 0$ and $U^l = 0$, the second and third rows and columns of $\mathbf{S}_{DRM}(\omega)$can be eliminated, as shown in Fig. 4(d). The reduced system can then be solved to obtain the nodal displacements. The transmittance response τ of the DRM structure in the y_g direction is determined as:

$$\tau = 20\log_{10}(|W(x) / W(0)|). \tag{18}$$

4. Characteristic analysis of defect states

This section begins with validation of the SEM model against finite element (FE) simulations. Subsequently, a parametric analysis is conducted to investigate how geometric parameters influence the low-frequency and broadband defect state characteristics of the DRM.

4.1. Validation of the SEM

In this subsection, validation of the previously developed SEM model is carried out using COMSOL 6.1, where the Timoshenko Beam interface is employed to simulate the rhombic-shaped truss structure. This interface accounts for shear deformation and rotary inertia, making it suitable for dynamic analyses of thick beams. For the finite-length structure, six unit cells are modeled, which satisfies the minimum requirement for bandgap formation [98]. Both the PRM and the DRM structures, corresponding to Case 1 and Case 2 in Section 2, are considered, with geometric and material parameters consistent with those in Table 1. The finite-length metamaterial is subjected to clamped-free boundary conditions. A time-harmonic force $F_y = F_x = F_0 e^{i\omega t}$ is exerted at one end to

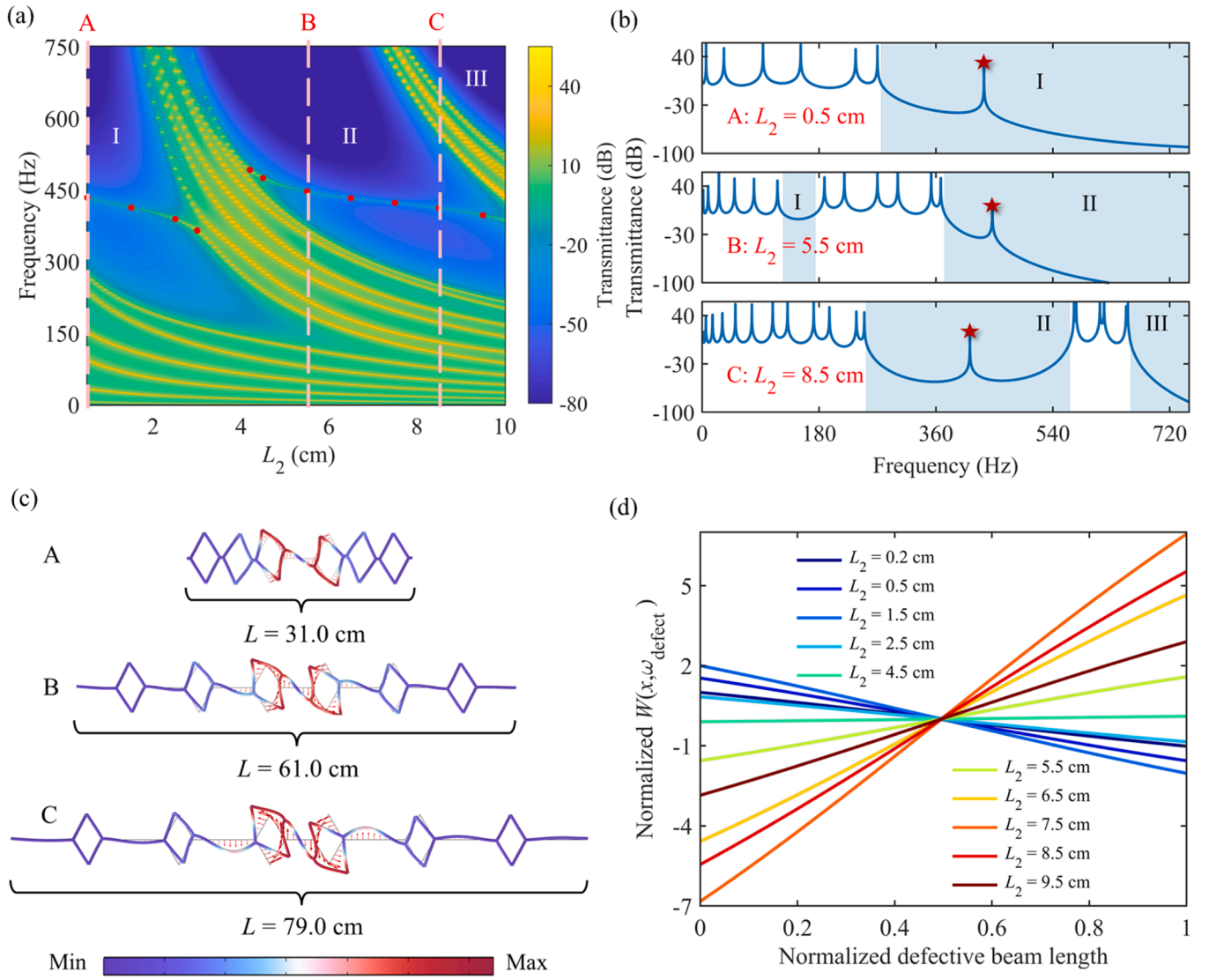

Fig. 7. (a) Heatmap of the DRM's transmittance versus L_2 (0.5 cm-9.5 cm), with defect-state peak marked by red dots; (b) Transmittance curves for slices A, B, and C in (a), with defect-state peaks highlighted by red pentagrams; (c) Mode shapes at the defect-state peak frequency for cases A, B and C, with the total DRM length L indicated; (d) Variation of the normalized vibration amplitude of the defective beam at the defect-state frequency with changing L_2.

excite flexural or longitudinal vibrations, and the displacement at the opposite end is recorded to compute the transmittance τ.

Fig. 5(a) and (b) present the transmittances of the PRM structure under F_y and F_x excitation, respectively, as obtained by the SEM and FE. In the FE results, both fine-mesh (112 elements) and coarse-mesh (57 elements) configurations are compared. The shaded regions in blue and pink indicate the flexural and longitudinal bandgaps, respectively. As shown in Fig. 5(a), the SEM predictions highly agree with the finely meshed FE results below 2000 Hz. By contrast, the coarse-mesh FE results deviate significantly from fine-mesh ones beyond the second-order Bragg bandgap, indicating reduced accuracy. This underscores the efficiency of SEM, which achieves high precision with fewer elements and degrees of freedom, thereby improving computational efficiency. However, discrepancies between SEM and finely meshed FE become more pronounced at higher frequencies. This behavior stems primarily from the breakdown of the long-wavelength approximation as the wavelength becomes comparable to the beam cross-section. In addition, localized three-dimensional deformation at joints and connections (for example, sectional warping, torsion-bending coupling, and local rotational inertia) becomes significant at higher frequencies but is not captured by Timoshenko beam models. Therefore, in this study, the SEM's predictive accuracy for the DRM is effectively limited to 2000 Hz. For frequencies above this threshold, finely meshed FE analysis is recommended, with element sizes on the order of one-eighth of the shortest target wavelength, and additional local refinement at joints to ensure adequate resolution of the smallest geometric features.

Furthermore, Fig. 5(c) and (d) present the dynamic response of the DRM structure with $L_3 = 4$ cm and $L_3 = 14$ cm, respectively. In Fig. 5(c), three distinct peaks, marked with pentagrams and labeled Da, Db, and Dc, emerge within the first three flexural bandgaps. These peaks correspond to defect states and align with the defect bands observed in Fig. 2(a). In Fig. 5(d), the elongated defective beam results in two defect state peaks, D1 and D2, within the first-order flexural bandgap, representing higher-order defect states, respectively. These results are consistent with those shown in Fig. 3(a).

Subsequently, we investigate the influence of three principal geometric parameters on the bandgap and defect-state characteristics of the DRM structure: the rhombic internal angle (α), the length of the connecting beam (L_2), and the defective beam (L_3). Specifically, the analysis focuses on how variations in these parameters affect the bandgap's center frequency and bandwidth, as well as the frequencies and number of defect states.

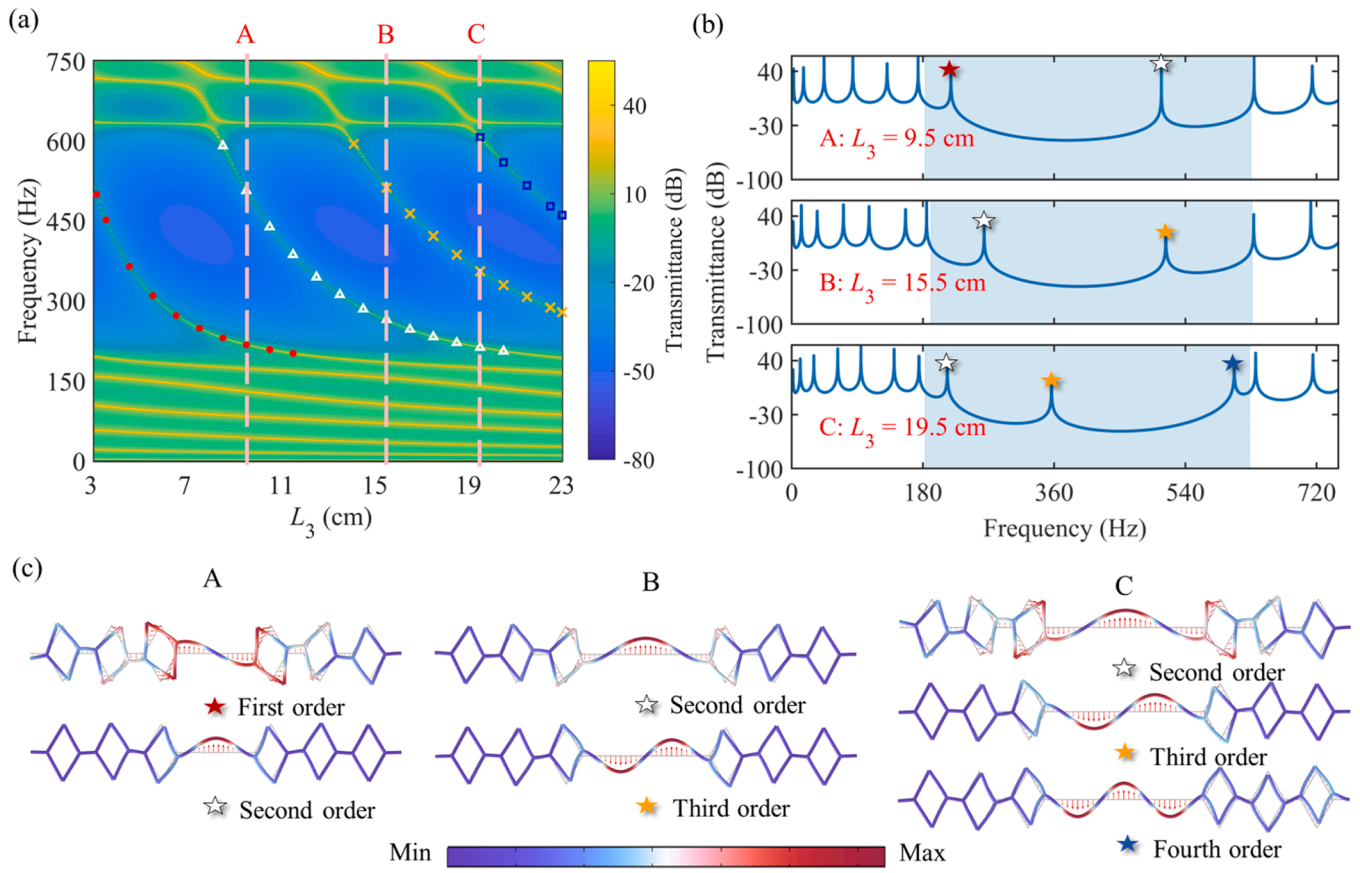

Fig. 8. (a) Heatmap of the DRM's transmittance versus L_3 (3 cm-23 cm), with the higher-order defect-state peaks marked by red dots, white triangles, orange forks, and blue squares; (b) Transmittance curves for slices A, B, and C in (a), with higher-order defect modes highlighted by red, white, orange and blue pentagrams; (c) Mode shapes at the defect-state peak frequency for cases A, B and C.

4.2. *Effect of rhombic internal angle*

Variations in the rhombic internal angle α substantially alter the lattice constant of the DRM structure, necessitating a systematic investigation of its dynamic response. Fig. 6(a) presents a heatmap of the DRM structure's transmittance as α varies from 10° to 80°. The blue shading denotes the bandgap, while the yellow contours trace the transmission peaks, with contours located inside the bandgap representing defect states. By analyzing mode shapes from FE simulations, we pinpointed the segments of these contours exhibiting vibrational localization and marked them with red dots. It can be seen that as α increases, the defect-state frequency first rises slightly and then gradually decreases, although the total variation remains small. To show more details, three representative cases are selected: A ($\alpha = 20°$), B ($\alpha = 50°$), and C ($\alpha = 75°$), as indicated by pink dashed lines in Fig. 6(a). Their corresponding transmittance are shown in Fig. 6(b), where the bandgap is shaded light blue, and defect-state peaks are denoted by red pentagrams. The associated mode shapes at each defect-state frequency are plotted in Fig. 6(c), clearly illustrating energy localization in the DRM. Two main observations can be drawn: (1) Increasing α shifts the bandgap toward higher frequencies, in agreement with Bragg scattering in an enlarged unit cell. Remarkably, the overall structure length at $\alpha = 75°$ is less than half that at $\alpha = 20°$, yet the lower band-edge frequency increases only marginally (from 162 Hz to 212.3 Hz). Moreover, the first and second Bragg bandgaps merge at large α (e.g., $\alpha = 75°$), producing a broader attenuation region. This suggests that large α enables compact designs to achieve wide, low-frequency vibration suppression; (2) although defect-state frequencies remain clustered near 400 Hz across all α, the defective beam's displacement amplitude diminishes as α grows. To quantify this, we calculate the displacement amplitude of the defective beam at the defect-state frequency ω_{defect} and normalize it to the result for $\alpha = 20°$. As shown in Fig. 6(d), the normalized displacement amplitude declines modestly up to $\alpha = 60°$ (e.g., to 0.82) and then falls more sharply at larger angles (e.g., to 0.27 at $\alpha = 75°$). This trend implies that excessively large α values can weaken energy localization and hinder defect-state excitation. To give a practical threshold of α, a standard engineering criterion is applied. For transduction/sensing applications, the harvested or detected power scales approximately with the square of the displacement amplitude. Thus, the -3 dB point (amplitude = 0.707×reference, i.e. 50% power loss) marks a practical performance threshold. Taking the defective beam's peak displacement at $\alpha = 20°$ as the reference, the threshold α_{th} is defined as:

$$\frac{A_{\text{def}}(\alpha_{\text{th}})}{A_{\text{def}}(20°)} = 0.707, \tag{19}$$

where $A_{\text{def}}(\alpha_{\text{th}})$ is the defective beam's displacement amplitude evaluated at ω_{defect} and numerical evaluation yields $\alpha_{\text{th}} = 67.4°$. For DRMs with different geometric or material parameters, the precise threshold α_{th} can be computed from Eq. (19).

4.3. *Effect of connecting beam length*

In this subsection, the variation of the DRM's system characteristics with the connecting-beam length L_2 is examined. All other parameters remain as in Table 1. Fig. 7(a) presents a heatmap of the transmittance versus L_2, where the first, second, and third Bragg bandgaps (shaded blue) are labeled I, II, and III, respectively. It can be seen that as L_2 increases, each bandgap shifts toward lower frequencies due to the enlarged lattice constant. Meanwhile, the bandgaps become narrower,

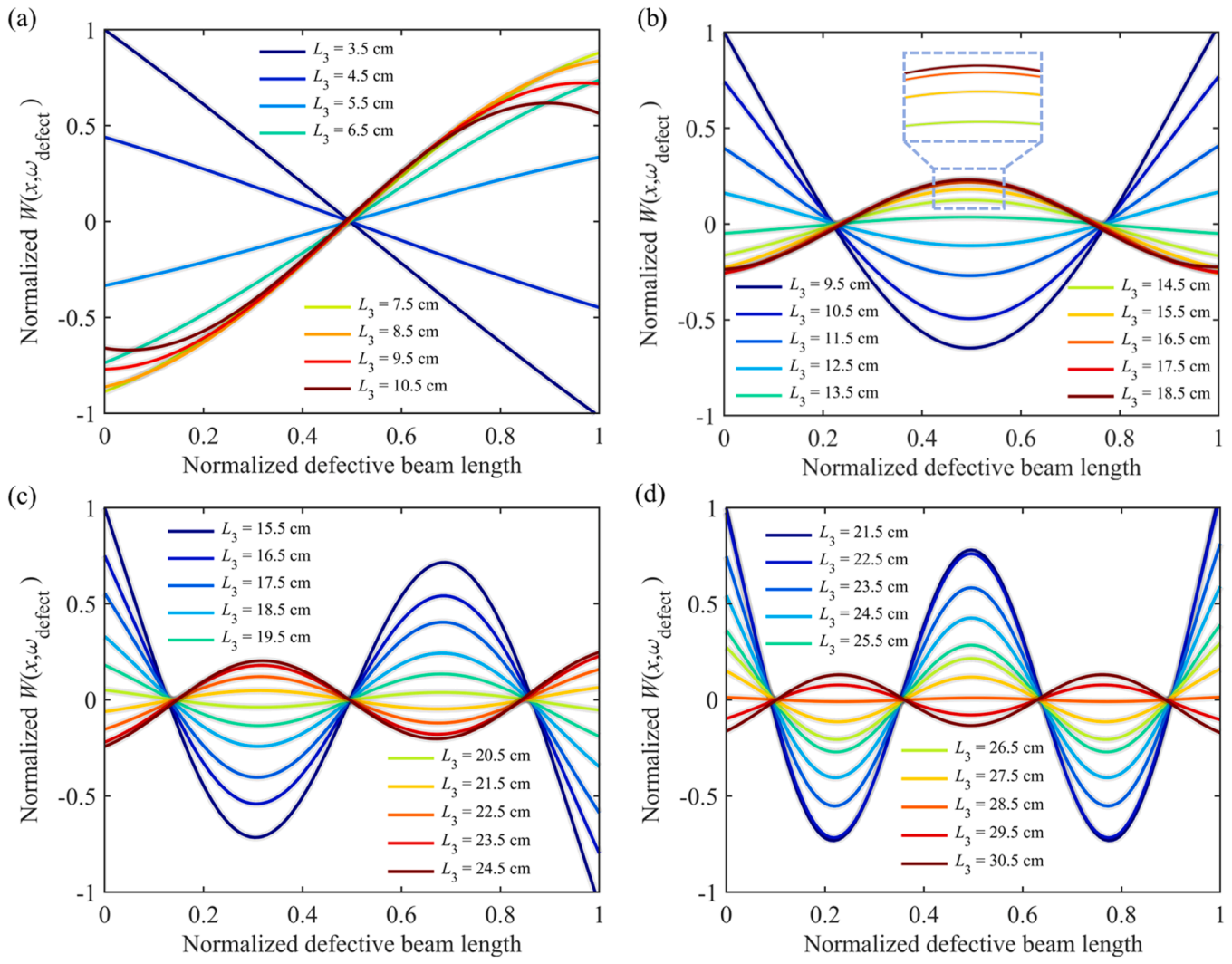

Fig. 9. Variation of the normalized vibration amplitude of the defective beam at the defect-state frequency with changing L_3: (a) First-order defect-state; (b) Second-order defect-state; (c) Third-order defect-state; (d) Fourth-order defect-state.

with a reduced vibration-attenuation strength (the blue shading lightens with L_2). For example, the first-order flexural bandgap shrinks from approximately 276.1 Hz-1282.6 Hz at $L_2 = 0.5$ cm to around 125.1 Hz-174 Hz at $L_2 = 5.5$ cm. The red-dotted regions mark the frequency ranges in which defect modes can emerge. Within both the first and second band gaps, the defect-state frequencies decrease slightly with L_2. Notably, for 3 cm $< L_2 <$ 4.5 cm, the defect states vanish because L_2 approaches the defective beam length L_3 (= 4 cm).

To examine these behaviors in detail, we extract three representative slices (A, B, and C) from Fig. 7(a) and plot their transmittance curves in Fig. 7(b). The plots clearly show that the first-order flexural bandgap progressively narrows, shifts to lower frequencies, and eventually disappears with increasing L_2. To understand how defect-mode localization evolves across different bandgap orders, Fig. 7(c) depicts the mode shapes corresponding to the three defect peaks in Fig. 7(b). In all cases, energy localizes around the defective beam in a dipole-like pattern, indicating that bandgap order does not alter the fundamental localization mechanisms. However, the intensity of localization differs among cases A-C. Fig. 7(d) quantifies this by comparing the normalized vibration amplitude of the defective beam (normalized to its amplitude at $L_2 = 0.2$ cm) at the defect-state frequency for varying L_2. It is observed that, for all bandgap orders, the defective-beam amplitude first rises and then falls as L_2 increases. Combining the results in Fig. 7(a), it is evident that energy localization diminishes as the defect-state frequency approaches the bandgap edges and intensifies when the frequency lies near the bandgap center. In addition, when the defect states fall into the second-order flexural bandgap, the corresponding mode shape reverses its phase. Therefore, to achieve optimal energy confinement, L_2 must be carefully tuned relative to the overall structure dimensions.

4.4. *Effect of defective beam length*

To explore how the defective beam length L_3 shapes system behavior, Fig. 8(a) shows a transmittance heatmap with varying L_3. All other parameters remain as in Table 1. The blue shaded area denotes the first-order flexural bandgap. It is seen that the bandgap's location and width remain essentially unchanged as L_3 varies. However, increasing L_3 gives rise to multiple, periodically spaced transmission peaks within the bandgap, corresponding to higher-order localized modes.

To distinguish, these mode branches are highlighted by red circles, white triangles, orange forks, and blue squares, respectively, which trace the continuous frequency ranges of the respective defect states. It can be seen that as L_3 increases, all four branches shift significantly toward lower-frequency regions, reflecting the reduction in effective stiffness associated with the longer defective beam. These tuning ranges span almost the entire bandgap and terminate near its boundaries. Properly designed bandgap region and defective beam length are expected to produce more low-frequency defect states.

Table 2
Geometric properties of the prototypes.

Prototype	L_1(cm)	L_2(cm)	L_3(cm)	α(°)	b(cm)	h(cm)
1	4	2	2	60	0.5	0.3
2	4	2	4	60	0.5	0.3
3	4	1	15	30	0.5	0.3

Moreover, the appearance of multiple marker sequences along the x-axis suggests that several defect states coexist within a single bandgap. To further illustrate this, Fig. 8(b) shows the transmittances extracted at slices A, B, and C from Fig. 8(a), with colored pentagrams marking the defect-state peaks. Cases A and B in Fig. 8(b) exhibit two peaks at (173.5, 507.3) Hz and (264.1, 513.2) Hz, respectively, while Case C shows three peaks at (174.5, 356.4, 607.4) Hz. The corresponding mode shapes shown in Fig. 8(b) are hereafter referred to as the first- through fourth-order defect states. Notably, the mode shape associated with the red pentagram in Fig. 8(b) is consistent with the dipole-like pattern analyzed in Section 2. As L_3 increases, the mode shapes of the defective beam resemble those of a clamped-clamped beam. This occurs because lengthening the beam reduces its natural frequencies and compresses their frequency spacing. When these eigenfrequencies fall within the bandgap, they become trapped and excited as higher-order defect states. For example, at $L_3 = 19.5$ cm, the eigenfrequencies are densely packed, allowing the formation of three distinct defect states.

Next, the influence of L_3 on the vibration amplitudes of the four defect states shown in Fig. 9 is investigated. Based on the SEM, the mode shapes of the defective beam at each defect-state frequency are obtained and normalized with respect to the amplitude at $L_3 = 3.5$ cm. It is clear that as L_3 increases, the vibration amplitudes of the defective beam at the first- through fourth-order defect-state frequencies initially decrease and then increase, accompanied by a 180° phase reversal. This behavior suggests that the vibrational localization effect can differ significantly among defect states of different orders for a fixed L_3, and that careful parameter selection is essential for achieving the desired localization characteristics.

Building on these insights, a general approach is summarized for engineering broad, low-frequency defect states. First, tailor the geometry of the rhombic metamaterial to reduce its effective stiffness, thereby lowering the bandgap frequency at a fixed lattice constant; and second, engineer the defective element to produce densely clustered natural frequencies, which promotes the formation of multiple localized modes within the low-frequency bandgap via the higher-order defect state mechanism. It should be noted that this mechanism is not confined to the first flexural bandgap but can be readily extended to the higher-order Bragg bandgaps. However, as higher-order bandgaps occur at higher frequencies and lie beyond the low-frequency objective of this study, detailed analyses are omitted.

5. Experimental validation

In this section, the fabrication of physical prototypes, the experimental measurement procedures, and the subsequent comparison with theoretical and numerical results are presented to validate the wide low-frequency defect state effects.

Three prototypes corresponding to the PRM and DRM structures are fabricated using 3D printing. Their geometric parameters are listed in Table 2. The prototypes are printed using Esun PLA ($E = 3.2$ GPa, $\rho = 1000$ kg/m^3, $\nu = 0.41$). The experimental setup is illustrated in Fig. 10(a). Each prototype is mounted vertically, with one end rigidly fixed to the shaker fixture to provide a clamped boundary condition, while the other end left free. A frequency-swept harmonic excitation is generated by a vibration controller (VibrationResearch, model: VR9500), amplified via a power amplifier (SignalForce, model: PA30E), and transmitted to a permanent magnet shaker (Labworks, model: ET-132-2). The resulting force, applied perpendicular to the surface of the metamaterial, has a constant acceleration amplitude of 0.5 G and a sweep rate of 60 Hz per minute, thereby exciting its flexural modes. The input signal is regulated by the VibrationVIEW 2021 software, while the data are recorded by the vibration controller. Two high-performance miniature ceramic accelerometers (PCB piezotronics, model: 352C23) are mounted at the clamped and free ends using wax. Before use, the accelerometers are calibrated using a reference standard accelerometer, and their sensitivities are determined to be 4.9 mV/g and 5.4 mV/g, respectively. With an extremely low mass of only 0.2 grams, these accelerometers impose minimal mass loading on the structure. To quantify the impact of the sensor-induced tip mass, Fig. 10(b) shows the DRM transmittance when a 0.2 g point mass is at the free end (structural and material parameters as in Fig. 5(c)). Compared with the mass-free counterpart, the added tip mass has a negligible effect on the DRM's dynamic response below 1500 Hz and produces slight downward shifts of the mode frequencies at higher frequencies. Thus, the sensor mass is deemed negligible for our sub-kilohertz defect-state analysis.

The measured transmittance of the PRM, designated as Prototype 1 (Fig. 11(a)), is presented in Fig. 11(b). For comparison, theoretical and numerical predictions from the SEM and FE models are included, with the bandgap regions shaded in blue. The experimental results show good agreement with the predictions in the first-order Bragg bandgap. However, the second-order bandgap obtained experimentally is narrower than expected, primarily due to more pronounced damping effects at higher frequencies and the greater influence of imperfect clamped boundary conditions on wave interference and diffraction. In addition, an unexpected transmission peak is observed at 661 Hz within the first bandgap, as indicated by the red dotted circle in Fig. 11(b). To verify that this is not related to a defect mode, acceleration responses are measured at three locations along the PRM under harmonic excitation at 661 Hz. Fig. 11(c) shows the sensor layout, with three accelerometers

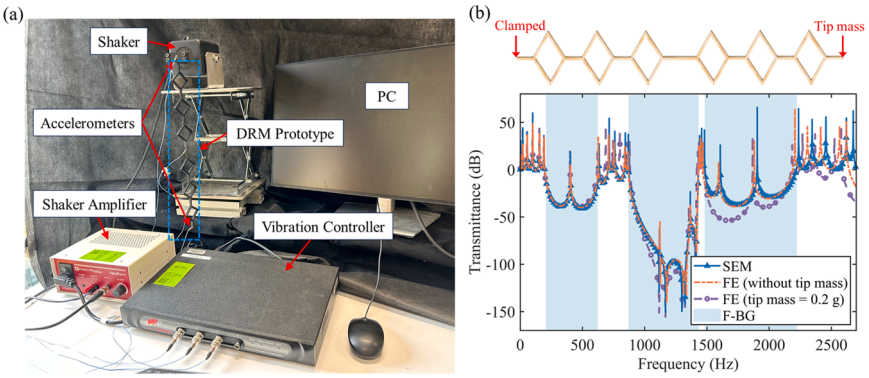

Fig. 10. (a) Experimental setup; (b) Comparison of transmittance with and without a tip mass. The tip mass of 0.2 g corresponds to the actual mass of the sensors (PCB piezotronics 352C23).

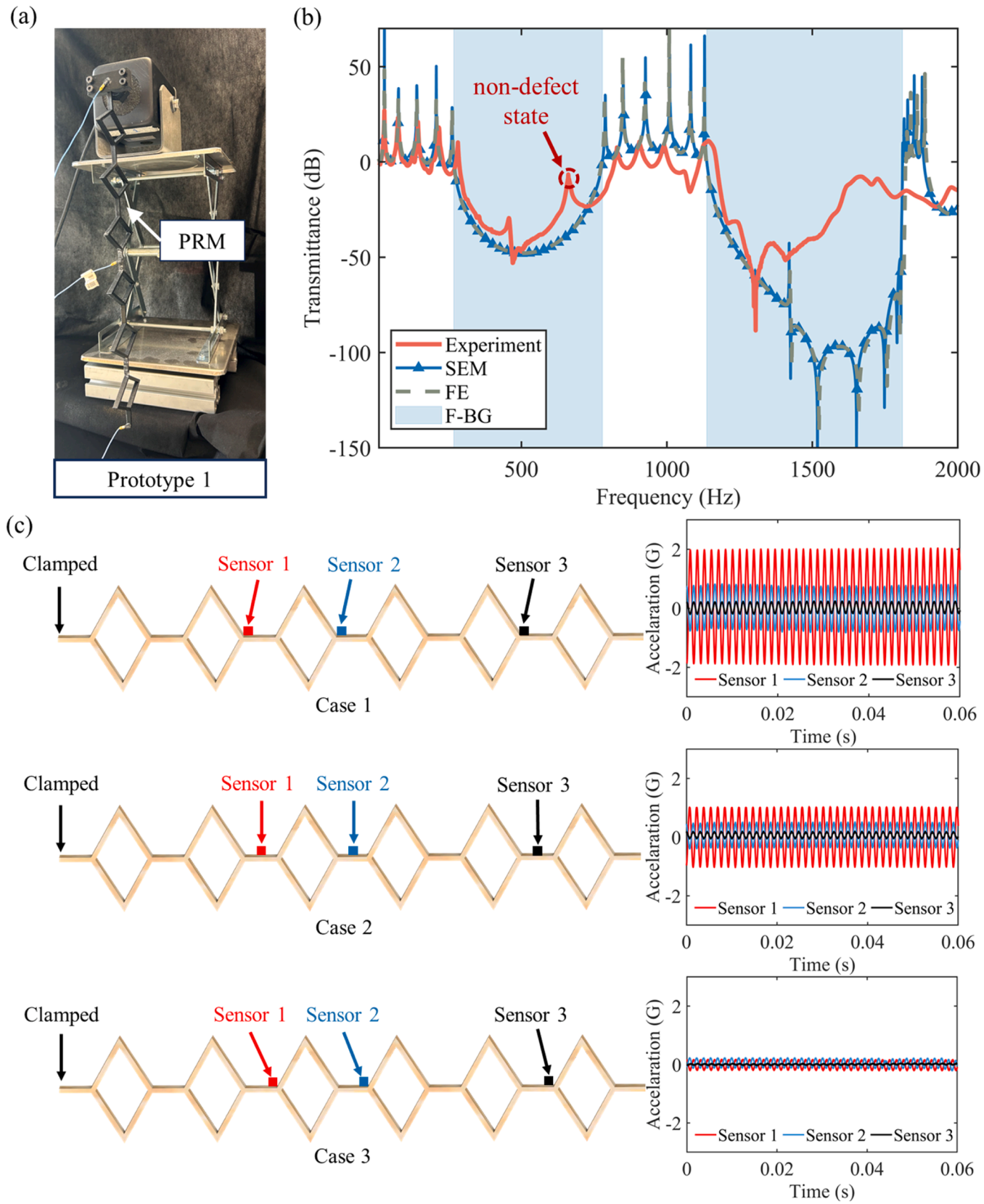

Fig. 11. (a) Prototype of the PRM; (b) Comparison of the measured transmittance with the predictions from SEM and FE models. The flexural bandgaps are indicated by blue shading; (c) Sensor layout and the corresponding acceleration measurements for sensor configuration Cases 1-3.

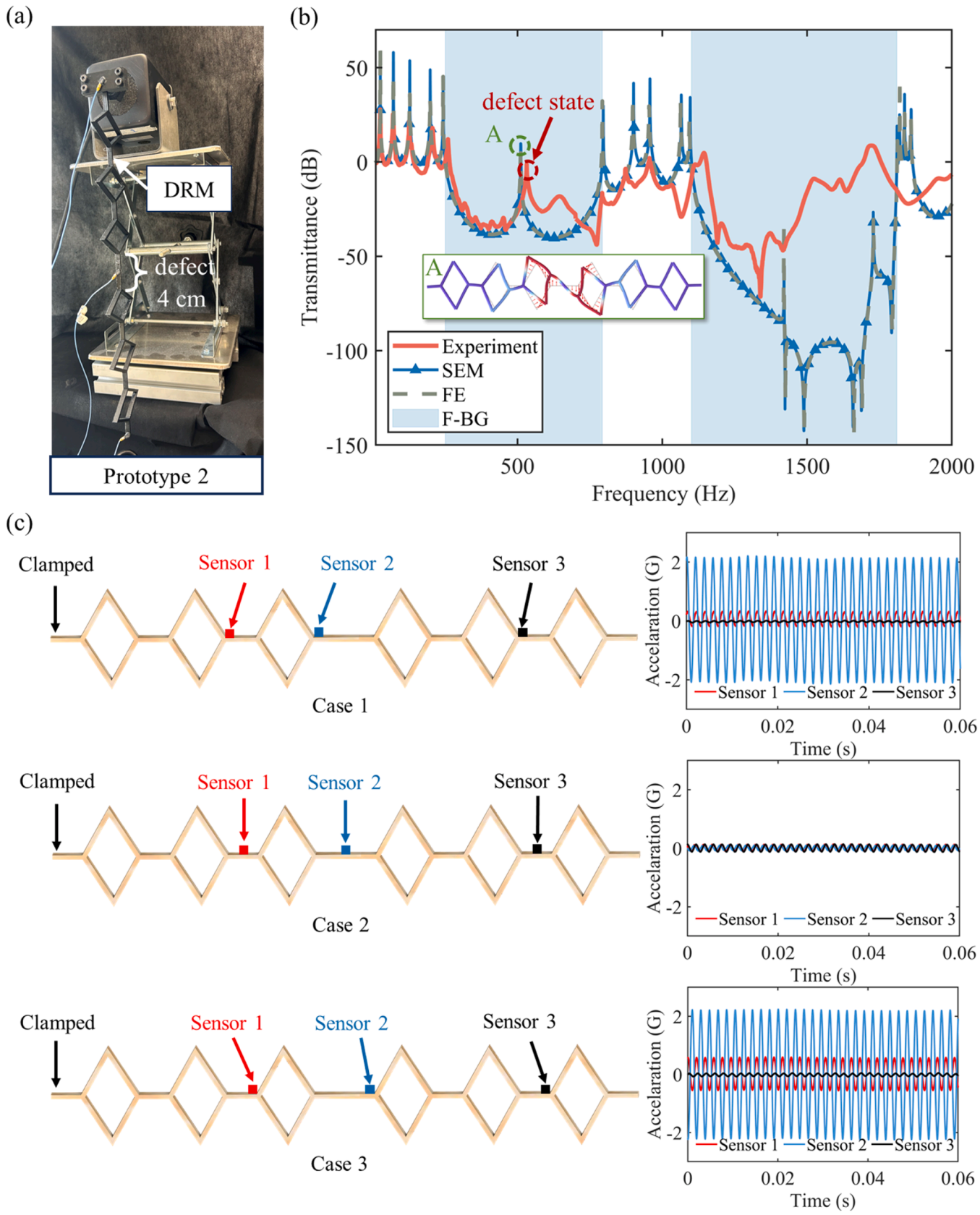

Fig. 12. (a) Prototype of the DRM; (b) Comparison of the measured transmittance with the predictions from SEM and FE models. The flexural bandgaps are indicated by blue shading; (c) Sensor layout and the corresponding acceleration measurements for sensor configuration Cases 1-3.

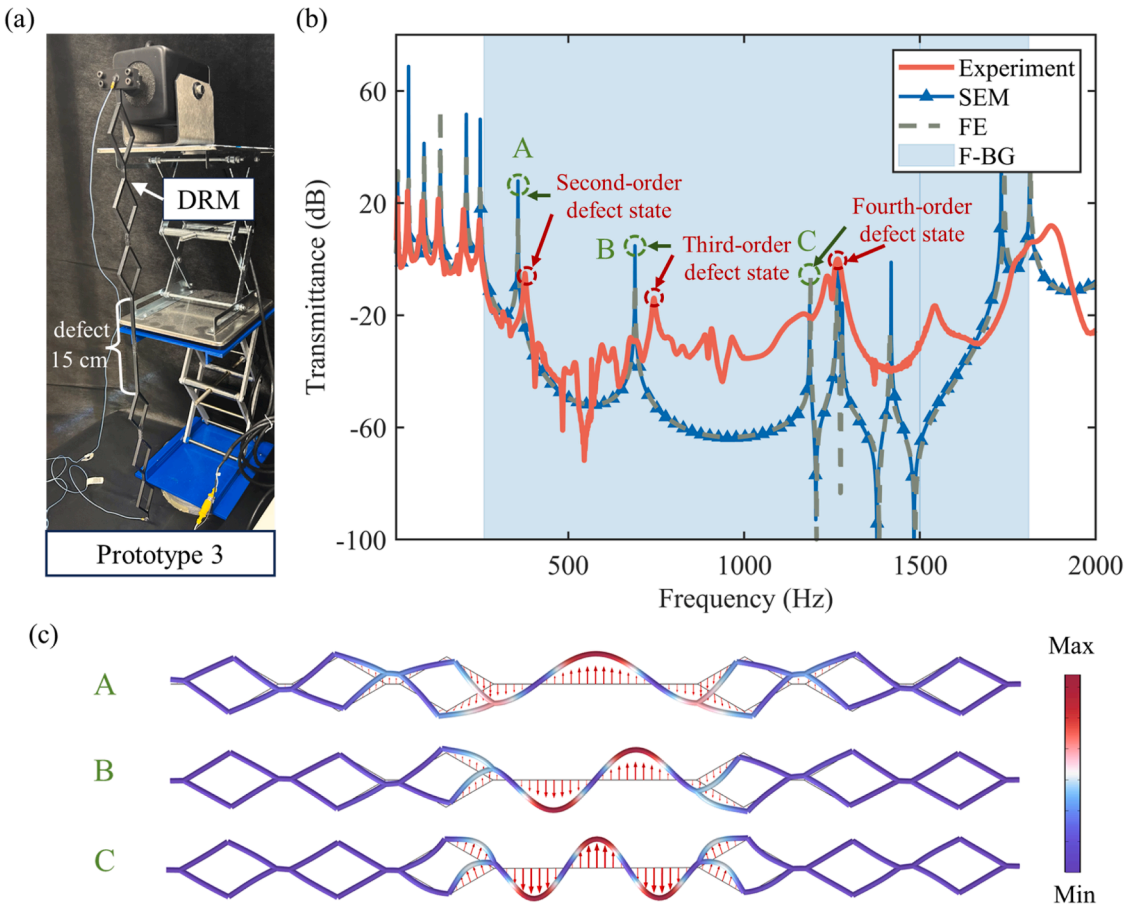

Fig. 13. Comparison of the measured transmittance of the prototype 3 with the predictions from SEM and FE models. The flexural bandgaps are indicated by blue shading.

Table 3
Measured and FE-predicted defect-state frequencies for prototypes 2-3.

Prototype	$f_{1,\,sim}$ (Hz)	$f_{1,\,exp}$ (Hz)	Δf_1	$f_{2,\,sim}$ (Hz)	$f_{2,\,exp}$ (Hz)	Δf_2	$f_{3,\,sim}$ (Hz)	$f_{3,\,exp}$ (Hz)	Δf_3
2	511	531.6	3.9%	/	/	/	/	/	/
3	357.7	375.5	4.7%	688.5	741.3	7.1%	1187	1267.8	6.4%

mounted on different connecting beams. To avoid missing a maximum amplitude because a sensor happened to be placed at a zero-displacement point, each sensor was tested at the left end, midspan, and right end of its connecting beam. The measured amplitudes, plotted in Fig. 11(c), show that the sensor nearest the excitation (i.e., sensor 1) recorded the largest amplitude and that amplitude decays with distance from the excitation. This spatial decay is consistent with normal wave propagation, with large amplitudes near the source that attenuate with distance, and does not indicate localized wave behavior.

Fig. 12(b) shows the measured transmittance of the DRM with $L_3 = 4$ cm (i.e., Prototype 2, as shown in Fig. 12(b)), which aligns well with the theoretical and numerical predictions. A distinct transmission peak appears at 531.6 Hz within the first bandgap, highlighted by the red dotted circle. This experimentally detected peak closely matches the SEM and FE predicted peak at around 511 Hz (green dashed circle). The FE-simulated mode shape corresponding to the predicted peak at 511 Hz is superimposed as inset B in Fig. 12(b). To further verify that the experimentally observed peak at 531.6 Hz corresponds to a defect state, the sensor layout and acceleration responses at three different connecting beams under harmonic excitation at this frequency are shown in Fig. 12(c). It is evident that Sensors 1 and 3, positioned outside the defective region, record consistently low amplitudes, indicating effective vibration suppression in the non-defective region. By contrast, Sensor 2, mounted on the defective beam, shows a strong response adjacent to the rhombic unit but much smaller amplitudes at the beam midspan. This spatial pattern matches the defect-mode shape in inset A of Fig. 12(b), confirming that vibrational energy is localized around the structural defect at 531.6 Hz. Moreover, the expected defect states within the second-order Bragg bandgap prove difficult to observe experimentally. We attribute this mainly to the damping of the PLA used, which typically has a loss factor of 0.02-0.04 [99]. Since the damping effect increases with frequency [100], resonance amplitudes at high frequencies are substantially attenuated, rendering the high-frequency defect states effectively unobservable. To achieve defect states above a few kilohertz, fabrication using lower-damping materials such as steel or aluminum is recommended. In addition, using a slower excitation sweep rate to avoid missing narrow peaks, and minimizing boundary friction with a stiff metal fixture and low-friction contact pads also help improve peak visibility.

Finally, prototype 3 is tested to examine multiple higher-order defect modes within the low-frequency bandgap. Its dimensions are optimized based on the parametric study in Section 4 to ensure strong energy localization. The results are shown in Fig. 13. The green dashed circles in Fig. 13(b) indicate the second-, third-, and fourth-order defect states,

and their corresponding mode shapes are illustrated in panels A-C of Fig. 13(c). Three distinct defect-state peaks appear clearly in the experimental transmittance, confirming the validity of the higher-order defect state concept proposed in this study. Table 3 summarizes the measured defect-state frequencies f_{exp} and the FE-predicted frequencies f_{sim} for prototypes 2 and 3. Subscripts 1-3 denote the defect states in order of increasing frequency. The difference between experiment and simulation is quantified by the relative error $\Delta f = |f_{exp} - f_{sim}| / f_{exp} \times 100\%$, validating the proposed DRM design.

The above experimental findings not only verify the theoretical and numerical predictions but also indicate the practical feasibility of the proposed DRM in real-world applications. With its lightweight yet robust lattice configuration, the DRM can be integrated into structural components such as sandwich cores, load-bearing panels, or embedded inserts in smart infrastructures. The multi-band low-frequency defect modes observed here match typical ambient vibration frequencies in engineering infrastructures, such as transport and aerospace systems. By placing piezoelectric transducers at the defect sites, the DRM can serve simultaneously as a structural element and an energy harvesting or sensing device. Building on these results, future work will explore the fabrication and dynamic performance of such multifunctional structures under realistic operating conditions.

6. Conclusions

This study tackles the challenge of broadband low-frequency vibration localization through the design of truss-based lattice metamaterials. A novel rhombus-shaped metamaterial with a single-point defect is proposed by selectively modifying the lengths of the connecting beams between rhombic units. The rhombic geometry reduces the structure's effective stiffness without altering the lattice scale, enabling low-frequency defect modes. Building on this, the concept of higher-order defect states is introduced, achieved by tuning multiple natural frequencies of the defective element into the bandgap range. These modes are captured via finite element-based band structure analysis. To enhance computational efficiency, a dynamic model based on the spectral element method is developed for accurate harmonic response prediction.

This work yields several valuable conclusions: First, defect states are highly sensitive to vibration polarization. Longitudinal waves interact weakly with the periodic lattice, making them difficult to localize. Second, defect modes can be generated within the lower-frequency Bragg bandgaps, with energy localization strength influenced by the rhombic angle and connecting beam length. Third, higher-order defect states are primarily governed by the intrinsic modes of the defective beam, independent of the bandgap order, and correspond to successive vibration modes of a clamped-clamped beam. Fourth, low-frequency higher-order defect states are experimentally validated for the first time, showing good agreement with both theoretical and numerical predictions. However, starting from the second-order bandgap, significant damping effects suppress defect-mode emergence, highlighting the importance of targeting low-frequency regions in defective metamaterial design.

Overall, this research presents a compact metamaterial design strategy for achieving multiple localized modes in the low-frequency regime, offering a new pathway for advanced vibration control and wave manipulation in engineering applications.

CRediT authorship contribution statement

Yupei Jian: Writing – original draft, Visualization, Methodology, Investigation, Funding acquisition, Formal analysis, Conceptualization. **Kexiang Wang:** Writing – review & editing, Methodology, Investigation. **Cuipeng Xia:** Writing – review & editing, Validation, Conceptualization. **Deqing Huang:** Writing – review & editing, Conceptualization. **Hesheng Han:** Writing – review & editing, Conceptualization. **Guobiao Hu:** Writing – review & editing, Supervision, Methodology, Conceptualization.

Declaration of competing interest

We declare that there is no conflict of interest between the authors

Acknowledgments

Yupei Jian would like to gratefully acknowledge the National Natural Science Foundation of China (Grant Nos. 52505130, 52305135), the Sichuan Science and Technology Program (Grant Nos. 2025ZNSFSC1268, 2025ZNSFSC1296), the China Postdoctoral Science Foundation (Grant No. 2024M762677), the Fundamental Research Funds for the Central Universities (Grant No. 2682024CX026) and the Nansha District Science and Technology Plan Project (Grant No. 2024ZD008).

Data availability

Data will be made available on request.

References

[1] Liu F-Y, Wang F-J, Zhao S-D. Negative elastic wave refraction and focusing regulation of single-phase solid phononic crystals. J Appl Phys 2024;135:163104.
[2] Beoletto P, Nistri F, Gliozzi A, Pugno N, Bosia F. Thin-lens equation in elasticity: imaging with gradient-index phononic crystals. Phys Rev Appl 2024;22:064054.
[3] Zhao C, Li Y, Deng Z, Wang Y, Zhang K. Negative refraction of elastic waves in two-dimensional inertial amplification metamaterials. Int J Mech Sci 2024;273:109325.
[4] Liu X, Chen S, Wang B, Tan X, Cao B, Yu L. A mechanical metamaterial with real-time tunable bandgap based on pneumatic actuation. Int J Mech Sci 2025;289:110045.
[5] Xiao L, Iqbal M, Yu X. Quasi-static band gaps in metamaterial pipes with negative stiffness resonators. Int J Mech Sci 2024;261:108668.
[6] Jian Y, Hu G, Tang L, Xu J, Huang D, Aw K. Graded metamaterial with broadband active controllability for low-frequency vibration suppression. J Appl Phys 2024;136:043108.
[7] Wang Z, Sun F, Xu X, Li X, Chen C, Lu M. Topological edge states in reconfigurable multi-stable mechanical metamaterials. Thin-Walled Struct 2024;202:112111.
[8] Chen K, Dong X, Peng Z, Meng G. Reconfigurable topological gradient metamaterials and potential applications. Thin-Walled Struct 2024;205:112572.
[9] Zhu D, Z-k Guo. Topological edge states in concave hexagonal gyroscope phononic crystals. J Acoust Soc Am 2025;157:4307–18.
[10] Montazeri A, Rahimi M, Park HS. Non-reciprocity and asymmetric elasticity in twisting chiral metamaterials. Int J Mech Sci 2025;287:109990.
[11] Auriemma F. Low-frequency non-reciprocal sound propagation features in thermoacoustic waveguide. J Acoust Soc Am 2024;156:314–25.
[12] Khan MB, Sugino C. Elastic nonreciprocity via nonreciprocal hybridization and destructive interference. Phys Rev Appl 2025;23:014028.
[13] Deng T, Zhao L, Jin F. Dual-functional perforated metamaterial plate for amplified energy harvesting of both acoustic and flexural waves. Thin-Walled Struct 2024;197:111615.
[14] Cao D-X, Li S-S, Guo X-Y, Chen X-M, Lai S-K. Buckling-driven piezoelectric defect-induced energy localization and harvesting using a Rubik's cube-inspired phononic crystal structure. Smart Mater Struct 2024;33:035036.
[15] Lee G, Lee S-J, Rho J, Kim M. Acoustic and mechanical metamaterials for energy harvesting and self-powered sensing applications. Mater Today Energy 2023;37:101387.
[16] Cao D-X, Li S-S, Zhan C-H, Lu Y-M, Mao J-J, Lai S-K. Defect-mode-induced energy localization/harvesting of a locally resonant phononic crystal plate: analysis of line defects. J Infrastr Intell Resilience 2022;1:100001.
[17] Li T, Wang Z, Xiao H, Yan Z, Yang C, Tan T. Dual-band piezoelectric acoustic energy harvesting by structural and local resonances of Helmholtz metamaterial. Nano Energy 2021;90:106523.
[18] Lee D, Youn BD, Jo S-H. Deep-learning-based framework for inverse design of a defective phononic crystal for narrowband filtering. Int J Mech Sci 2023;255:108474.
[19] Zhang X, Li Y, Wang Y, Jia Z, Luo Y. Narrow-band filter design of phononic crystals with periodic point defects via topology optimization. Int J Mech Sci 2021;212:106829.
[20] Jian Y, Tang L, Hu G, Li Z, Aw KC. Design of graded piezoelectric metamaterial beam with spatial variation of electrodes. Int J Mech Sci 2022;218:107068.
[21] Jian Y, Hu G, Tang L, Tang W, Abdi M, Aw KC. Analytical and experimental study of a metamaterial beam with grading piezoelectric transducers for vibration attenuation band widening. Eng Struct 2023;275:115091.

[22] Xiao J, Ding X, Huang W, He Q, Shao Y. Rotating machinery weak fault features enhancement via line-defect phononic crystal sensing. Mech Syst Signal Process 2024;220:111657.
[23] Shu Z, Zhang G, Cong Y, Gu S. Size effects on a one-dimensional defective phononic crystal sensor. Smart Materials and Structures 2023;32:115029.
[24] Sim MS, You KY, Dewan R, Esa F, Salim MR, Khe CS, et al. Microwave sensors loaded with metamaterial-inspired resonators for dielectric material characterization: A review. Sensors Actuat A: Phys 2024;372:115322.
[25] Zheng K, Zhu J, Chen J, Hameed MS, Chen J, Li Z. Damage detection method based on defect mode for orthogonal grid stiffened panels. Eng Struct 2023;279:115636.
[26] Gao F, Benchabane S, Bermak A, Dong S, Khelif A. On-chip tightly confined guiding and splitting of surface acoustic waves using line defects in phononic crystals. Adv Funct Mater 2023;33:2213625.
[27] Oudich M, Gerard NJ, Deng Y, Jing Y. Tailoring structure-borne sound through bandgap engineering in phononic crystals and metamaterials: a comprehensive review. Adv Funct Mater 2023;33:2206309.
[28] Jiang Z, Zhou Y, Zheng S, Liu J, Xia B. Waveguides induced by replacing defects in phononic crystal. Int J Mech Sci 2023;255:108464.
[29] Zaiser M, Zapperi S. Disordered mechanical metamaterials. Nature Rev Phys 2023;5:679–88.
[30] Hu G, Tang L, Liang J, Lan C, Das R. Acoustic-elastic metamaterials and phononic crystals for energy harvesting: A review. Smart Mater Struct 2021;30:085025.
[31] Hosseinkhani A, Ebrahimian F, Younesian D, Moayedizadeh A. Defected meta-lattice structures for the enhanced localized vibrational energy harvesting. Nano Energy 2022;100:107488.
[32] Lan C, Zhang Y, Wang S, Lu Y, Wang Y, Hu G. Enhancing galloping-based energy harvesting through expanded quasi-zero-stiffness region. Smart Mater Struct 2025;34:055018.
[33] Zhong J, Chai Z, Xiang J. Double defects in trampoline effect and Helmholtz coupled acoustic metamaterial for broadband piezoelectric energy harvesting. Wave Motion 2024;124:103248.
[34] Hyun J, Jung J, Park J, Choi W, Kim M. Simultaneous low-frequency vibration isolation and energy harvesting via attachable metamaterials. Nano Converg 2024;11:38.
[35] Shao H, Chen G, He H. Elastic wave localization and energy harvesting defined by piezoelectric patches on phononic crystal waveguide. Phys Letters A 2021;403:127366.
[36] Ma K, Tan T, Yan Z, Liu F, Liao W-H, Zhang W. Metamaterial and Helmholtz coupled resonator for high-density acoustic energy harvesting. Nano Energy 2021;82:105693.
[37] Wu B, Jiang W, Jiang J, Zhao Z, Tang Y, Zhou W, et al. Wave manipulation in intelligent metamaterials: recent progress and prospects. Adv Funct Mater 2024;34:2316745.
[38] Qi S, Oudich M, Li Y, Assouar B. Acoustic energy harvesting based on a planar acoustic metamaterial. Appl Phys Lett 2016;108:263501.
[39] Sun W, Zhong K, Liu Y, Xiao H, Zhao D, Yan Z, et al. Enhanced metamaterial vibration for high-performance acoustic piezoelectric energy harvesting. Compos Commun 2022;35:101342.
[40] Jo S-H, Yoon H, Shin YC, Choi W, Park C-S, Kim M, et al. Designing a phononic crystal with a defect for energy localization and harvesting: supercell size and defect location. Int J Mech Sci 2020;179:105670.
[41] Park C-S, Shin YC, Jo S-H, Yoon H, Choi W, Youn BD, et al. Two-dimensional octagonal phononic crystals for highly dense piezoelectric energy harvesting. Nano Energy 2019;57:327–37.
[42] Jo S-H, Yoon H, Shin YC, Youn BD. An analytical model of a phononic crystal with a piezoelectric defect for energy harvesting using an electroelastically coupled transfer matrix. Int J Mech Sci 2021;193:106160.
[43] Cai C, Wang Z, Chu Y, Liu G, Xu Z. The phononic band gaps of Bragg scattering and locally resonant pentamode metamaterials. J Phys D Appl Phys 2017;50:415105.
[44] Xiao P, Miao L, Zheng H, Lei L. Low frequency vibration reduction bandgap characteristics and engineering application of phononic-like crystal metaconcrete material. Constr Build Mater 2024;411:134734.
[45] Dong P, Hu J, Li Y, Gong Z, Li G, Liu Y, et al. Cementitious metamaterials for low-frequency vibration suppression: inverse design and performance analysis. Constr Build Mater 2025;476:141308.
[46] Yin P, Tang L, Li Z, Xia C, Li Z, Aw KC. Harnessing ultra-low-frequency vibration energy by a rolling-swing electromagnetic energy harvester with counter-rotations. Appl Energy 2025;377:124507.
[47] Oudich M, Li Y. Tunable sub-wavelength acoustic energy harvesting with a metamaterial plate. J Phys D Appl Phys 2017;50:315104.
[48] Bian L-a, Deng Z, Hong Y, Qiu Y, Liu Z, Xiao P, et al. Double-mode absorption in double-defect photonic crystal with one graphene multilayer. Opt Quantum Electron 2020;52:1–10.
[49] Geng Q, Wang T, Wu L, Li Y. Defect coupling behavior and flexural wave energy harvesting of phononic crystal beams with double defects in thermal environments. J Phys D Appl Phys 2021;54:225501.
[50] Jo S-H, Shin YC, Choi W, Yoon H, Youn BD, Kim M. Double defects-induced elastic wave coupling and energy localization in a phononic crystal. Nano Converg 2021;8:27.
[51] Zhang G-Y, Liu Z-J, Zhang Y, Wu L, Li Z-G, Zhang C-R, et al. Phononic crystals with decoupled different defects enhance energy localization and harvesting performance. J Acoust Soc Am 2025;157:2697–708.
[52] Chen Q, Zhu Y, Zhang K, Feng K. Broadband low-frequency acoustic energy harvesting amplified by sonic crystal metamaterial with double defects. J Vibration Eng Technol 2024;12:469–80.
[53] Xiang H, Chai Z, Kou W, Zhong H, Xiang J. An investigation of the energy harvesting capabilities of a novel three-dimensional super-cell phononic crystal with a local resonance structure. Sensors 2024;24:361.
[54] Lee G, Park J, Choi W, Ji B, Kim M, Rho J. Multiband elastic wave energy localization for highly amplified piezoelectric energy harvesting using trampoline metamaterials. Mech Syst Signal Process 2023;200:110593.
[55] Xiao H, Tan T, Li T, Zhang L, Yuan C, Yan Z. Enhanced multi-band acoustic energy harvesting using double defect modes of Helmholtz resonant metamaterial. Smart Mater Struct 2023;32:105030.
[56] Thomes RL, Beli D, Sugino C, Erturk A, Junior CDM. Programmable moving defect for spatiotemporal wave localization in piezoelectric metamaterials. Phys Rev Appl 2023;19:064031.
[57] Jo S-H, Park M, Kim M, Yang J. Tunable bandpass filters using a defective phononic crystal shunted to synthetic negative capacitance for longitudinal waves. J Appl Phys 2024;135:164502.
[58] Thomes RL, Beli D, Junior CDM. Space–time wave localization in electromechanical metamaterial beams with programmable defects. Mech Syst Signal Process 2022;167:108550.
[59] Hao Y, Huo Y, Zhang W. Locally resonant metamaterial plate with cantilever spiral beam-mass resonators and various piezoelectric defects for energy harvesting. Thin-Walled Structures 2025;213:113259.
[60] Zhang S, Bian X. Tunable defect states of flexural waves in magnetostrictive phononic crystal beams by magneto-mechanical-thermal coupling loadings. Thin-Walled Structures 2024;199:111848.
[61] Zhang S, Su L. Multi-field induced reconfigurable point defect state of flexural waves in magnetostrictive phononic crystals plates. Mech Mater 2025;208:105415.
[62] Jian Y, Tang L, Huang D, Han H, Liu W, Hu G. Designing an electromechanical metamaterial beam with arbitrary decoupled defect modes for multi-band wave localization. Smart Mater Struct 2025;34:035015.
[63] Geng Q, Fong P-K, Ning J, Shao Z, Li Y. Thermally-induced transitions of multi-frequency defect wave localization and energy harvesting of phononic crystal plate. Int J Mech Sci 2022;222:107253.
[64] Geng Q, Cai T, Li Y. Flexural wave manipulation and energy harvesting characteristics of a defect phononic crystal beam with thermal effects. J Appl Phys 2019;125:035103.
[65] Guo J, Li Y, Xiao Y, Fan Y, Yu D, Wen J. Multiscale modeling and design of lattice truss core sandwich metastructures for broadband low-frequency vibration reduction. Compos Struct 2022;289:115463.
[66] Vo NH, Pham TM, Bi K, Hao H. Model for analytical investigation on meta-lattice truss for low-frequency spatial wave manipulation. Wave Motion 2021;103:102735.
[67] Jiang G, Zang H, Xiong Y, Shen Y, Guo Z, Yang Y, et al. Design and vibration reduction performance analysis of a 6-DOF nonlinear vibration isolation platform by employing bio-inspired multi-joint X-structure. Nonlinear Dyn 2025;113:21119.
[68] Sun Y, Zhang G, Lee HP, Zheng H, Luo Z, Li F. Sound transmission of truss-based X-shaped inertial amplification metamaterial double panels. Int J Mech Sci 2024;283:109669.
[69] Wu Z, Li F, Zhang C. Band-gap analysis of a novel lattice with a hierarchical periodicity using the spectral element method. J Sound Vib 2018;421:246–60.
[70] Li Y, Li H, Liu X, Yan S. Bandgap and wave propagation of spring–mass–truss elastic metamaterial with a scissor-like structure. J Phys D Appl Phys 2021;55:055303.
[71] Meng J, Deng Z, Zhang K, Xu X, Wen F. Band gap analysis of star-shaped honeycombs with varied Poisson's ratio. Smart Mater Struct 2015;24:095011.
[72] Mwema FM, Wambua JM, Igwe AC, Akinlabi SA, Jen TC, Akinlabi E. Mechanical response of four-star-honeycomb hybrid metamaterial under In-plane loading. Adv Eng Mater 2025;27:2401886.
[73] Gao N, Wei Z, Hou H, Krushynska AO. Design and experimental investigation of V-folded beams with acoustic black hole indentations. J Acoust Soc Am 2019;145:EL79–83.
[74] Song B-X, Guo J-G, Qu C, Wang Z-Y. Design and analysis of a novel star-shaped auxetic cylindrical metamaterial with excellent mechanical performance. Eng Struct 2025;332:120047.
[75] Masoodi AR, Ghandehari MA, Tornabene F, Dimitri R. Natural frequency response of FG-CNT coupled curved beams in thermal conditions. Appl Sci 2024;14:687.
[76] Ghandehari MA, Masoodi AR, Panda SK. Thermal frequency analysis of double CNT-reinforced polymeric straight beam. J Vibration Eng Technol 2024;12:649–65.
[77] Belyaev A, Tovstik P, Tovstik T. Thin rod under longitudinal dynamic compression. Mech Solids 2017;52:364–77.
[78] Guo Z, Hu G, Sorokin V, Tang L, Yang X, Zhang J. Low-frequency flexural wave attenuation in metamaterial sandwich beam with hourglass lattice truss core. Wave Motion 2021;104:102750.
[79] He F, Zhang Y, Qian D, Wei G. Band gap properties of a curved phononic crystal truss structure. Acta Mech 2025;236:2193–209.
[80] Guo Z, Wen J, Shen Y, Hu G, Jiang G. Band folding induced broadband vibration suppression of star-shaped metamaterials: theory and experiment. Thin-Walled Structures 2024;198:111756.

[81] Rong B, Lu K, Ni X, Ge J. Hybrid finite element transfer matrix method and its parallel solution for fast calculation of large-scale structural eigenproblem. Appl Math Model 2020;77:169–81.
[82] Mottaghi H, Masoodi AR, Gandomi AH. Multiscale analysis of carbon nanotube-reinforced curved beams: A finite element approach coupled with multilayer perceptron neural network. Results Eng 2024;23:102585.
[83] Tong C, Liu J, Liu QH. Mixed finite element numerical mode matching method for designing infrared broadband polarization-independent metamaterial absorbers. Opt Express 2022;30:45031–42.
[84] Zhu J, Zhang R, Wang K, Zheng L, Chen T, Ding W. Flexural-wave dual bandgaps in elastic metamaterial beam based on L-shaped local resonators. Appl Acoust 2025;235:110692.
[85] Hua F, You Q, Huang Q, Fu W, Zhou X. Exploring guided wave propagation in composite cylindrical shells with an embedded delamination through refined spectral element method. Thin-Walled Struct 2024;194:111326.
[86] Bao Y, Yao Z, Hu X, Liu X, Shan Y, He T. Complete bandgap of three-dimensional helical metamaterial tapered rod with power-law radius. Mech Syst Signal Process 2024;211:111257.
[87] H-y Yang, S-l Cheng, X-f Li, Yan Q, Wang B, Y-j Xin, et al. Ultra-low-frequency multi-broadband and vibration suppression mechanism of innovative star-shaped hybrid metamaterials. Mater Des 2023;230:111966.
[88] Jin Y, Jia X-Y, Wu Q-Q, He X, Yu G-C, Wu L-Z, et al. Design of vibration isolators by using the Bragg scattering and local resonance band gaps in a layered honeycomb meta-structure. J Sound Vib 2022;521:116721.
[89] Zhang X, Li Y, Wang Y, Luo Y. Ultra-wide low-frequency bandgap design of acoustic metamaterial via multi-material topology optimization. Compos Struct 2023;306:116584.
[90] Tang R, Lu T, Zheng W. Low-frequency ultrawide band gap study of symmetric conical scatterer phononic crystal. J Vibr Eng Technol 2024;12:3667–76.
[91] Mi Y, Cheng L, Zhai W, Yu X. Broadband low-frequency sound attenuation in duct with embedded periodic sonic black holes. J Sound Vib 2022;536:117138.
[92] Bergamini A, Miniaci M, Delpero T, Tallarico D, Van Damme B, Hannema G, et al. Tacticity in chiral phononic crystals. Nat Commun 2019;10:4525.
[93] Liu Y, Yang J, Yi X, Guo W, Feng Q, Chronopoulos D. Enhanced vibration suppression using diatomic acoustic metamaterial with negative stiffness mechanism. Eng Struct 2022;271:114939.
[94] Liu T, Fan Y-X, Zhang J-Y, Su Y, Tao Z-Y. Interface states of dipole-like distributions in a quasi-periodic acoustic waveguide. Appl Acoust 2021;181:108174.
[95] Jo S-H, Youn BD. A phononic crystal with differently configured double defects for broadband elastic wave energy localization and harvesting. Crystals (Basel) 2021;11:643.
[96] Wu Z-J, Li F-M, Zhang C. Vibration properties of piezoelectric square lattice structures. Mech Res Commun 2014;62:123–31.
[97] Wu Z-J, Li F-M, Zhang C. Vibration band-gap properties of three-dimensional Kagome lattices using the spectral element method. J Sound Vib 2015;341:162–73.
[98] Sugino C, Leadenham S, Ruzzene M, Erturk A. An investigation of electroelastic bandgap formation in locally resonant piezoelectric metastructures. Smart Mater Struct 2017;26:055029.
[99] Dunaj P, Berczyński S, Miądlicki K, Irska I, Niesterowicz B. Increasing damping of thin-walled structures using additively manufactured vibration eliminators. Materials (Basel) 2020;13:2125.
[100] Bera KK, Biswas S, Banerjee A. Optimized piezo-shunted metadamping towards the high-stiff high-damped metamaterial. J Intell Mater Syst Struct 2024;35:705–17.